Heterostructure Boosts a Noble-metal-free Oxygen-evolving Electrocatalyst in Acid

Part 1: Supplementary Figures:
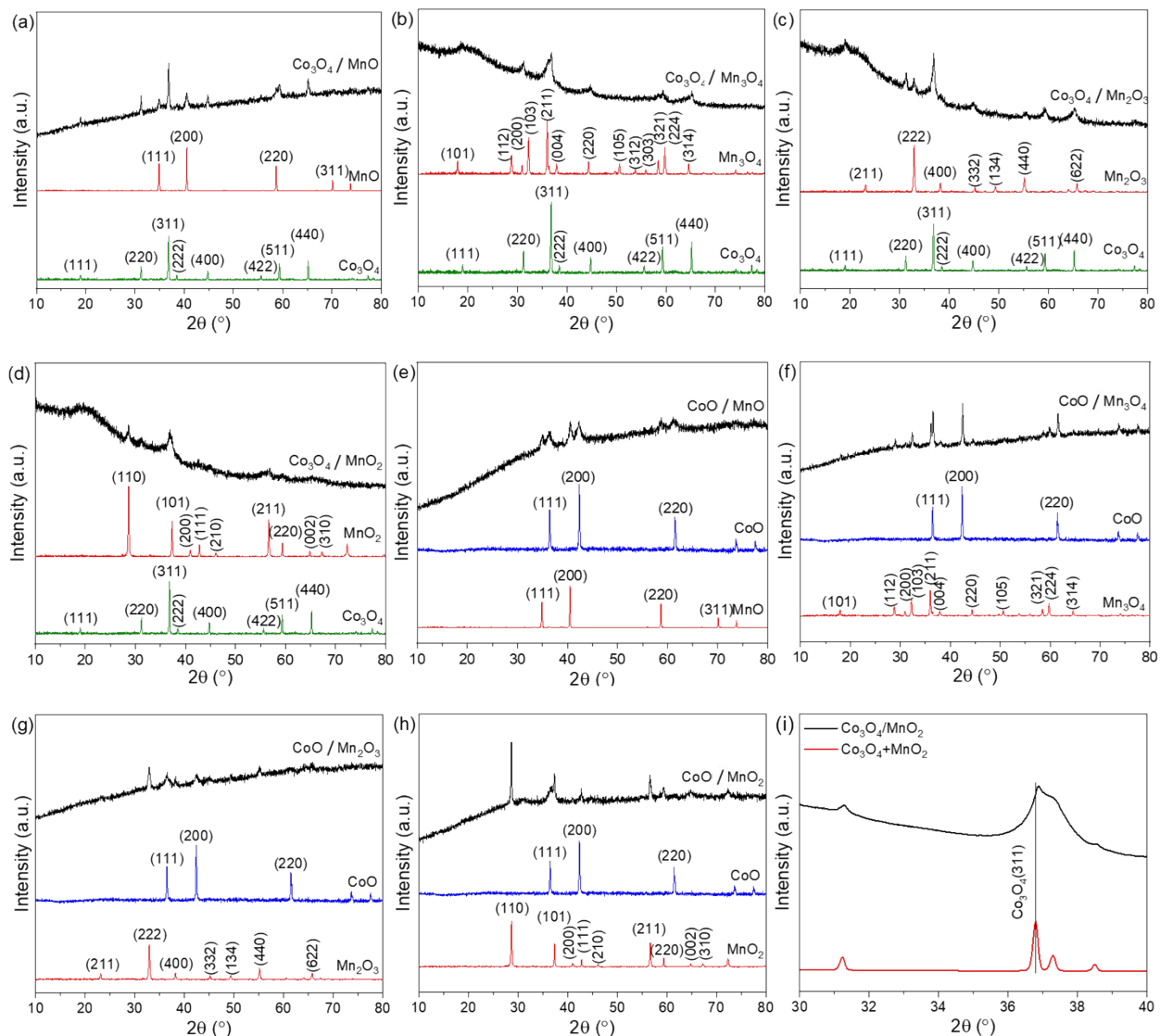
(1)

Figure S1. (a)-(h) XRD patterns of different hybridized CoO_x/MnO_x. Compared with those of pristine CoO_x and MnO_x, the diffraction peaks of CoO_x/MnO_x are generally broader, which might be attributed to the reduced crystallite size and hybridization-formed heterostructures. (i) Synchrotron XRD comparison between Co_3O_4/MnO_2 and $Co_3O_4+MnO_2$.
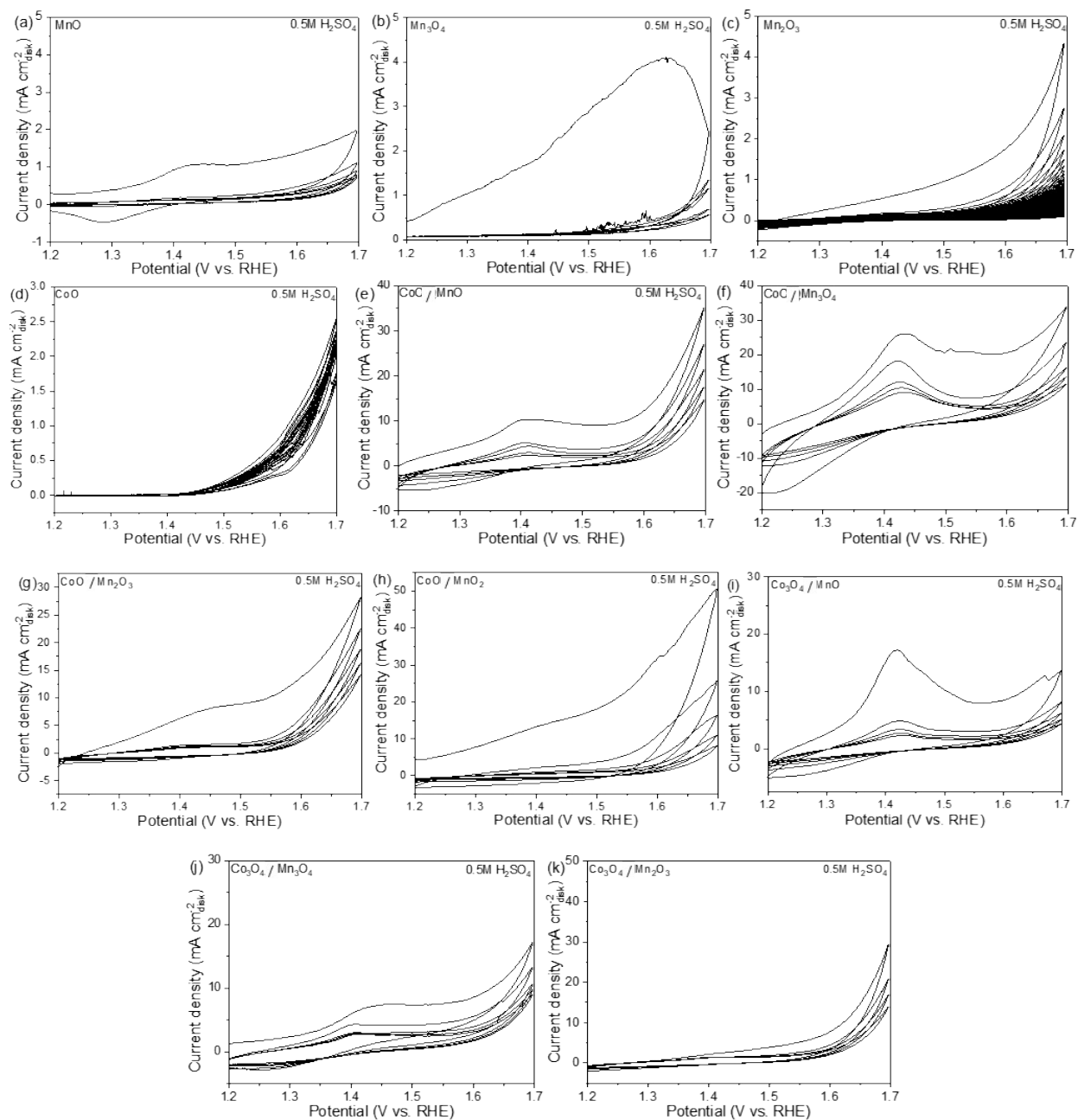
(2)

Figure S2. CV curves in 0.5M H₂SO₄. No IR correction was applied for the polarization potential.

(3)

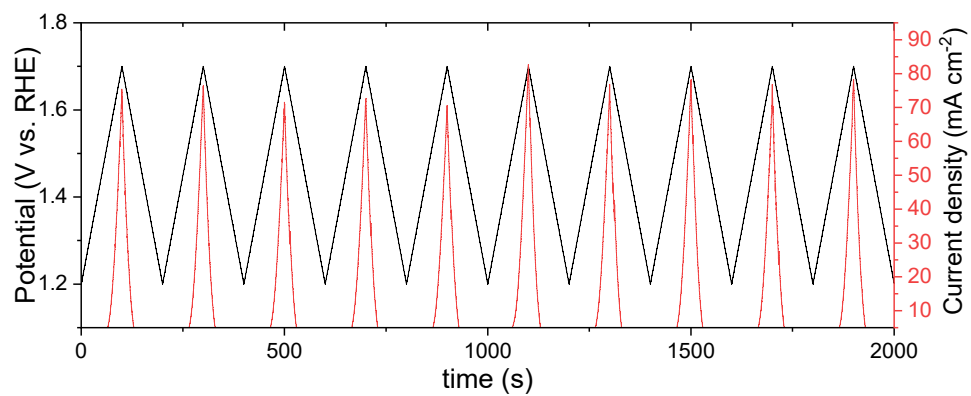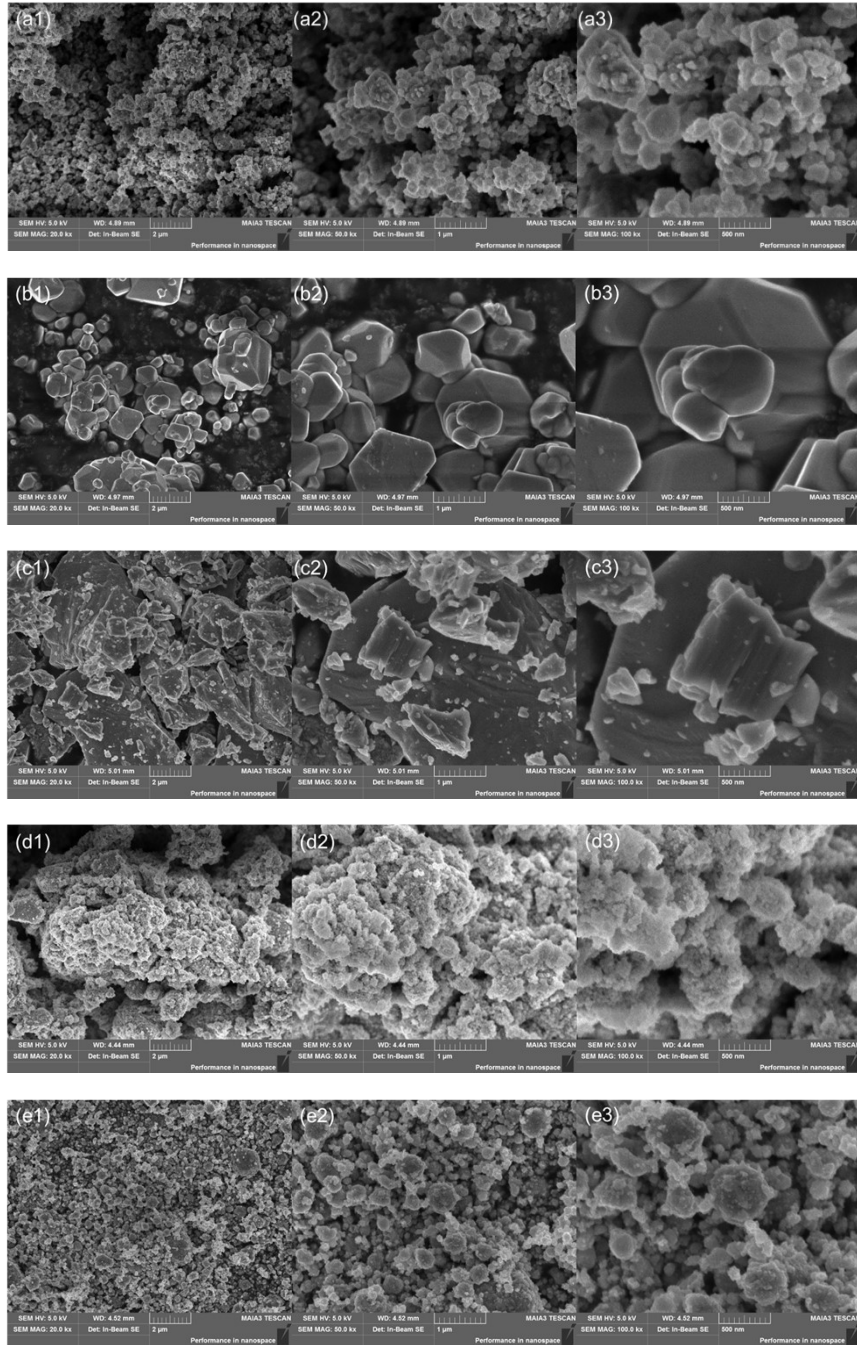**Figure S3**. Time-dependent CV scans for Co_3O_4/MnO_2: the black color curve represents potential while the red-color curve corresponds to the current density.
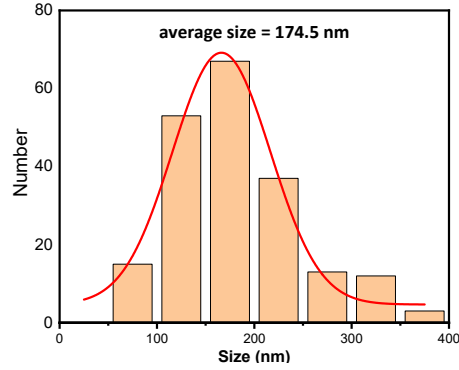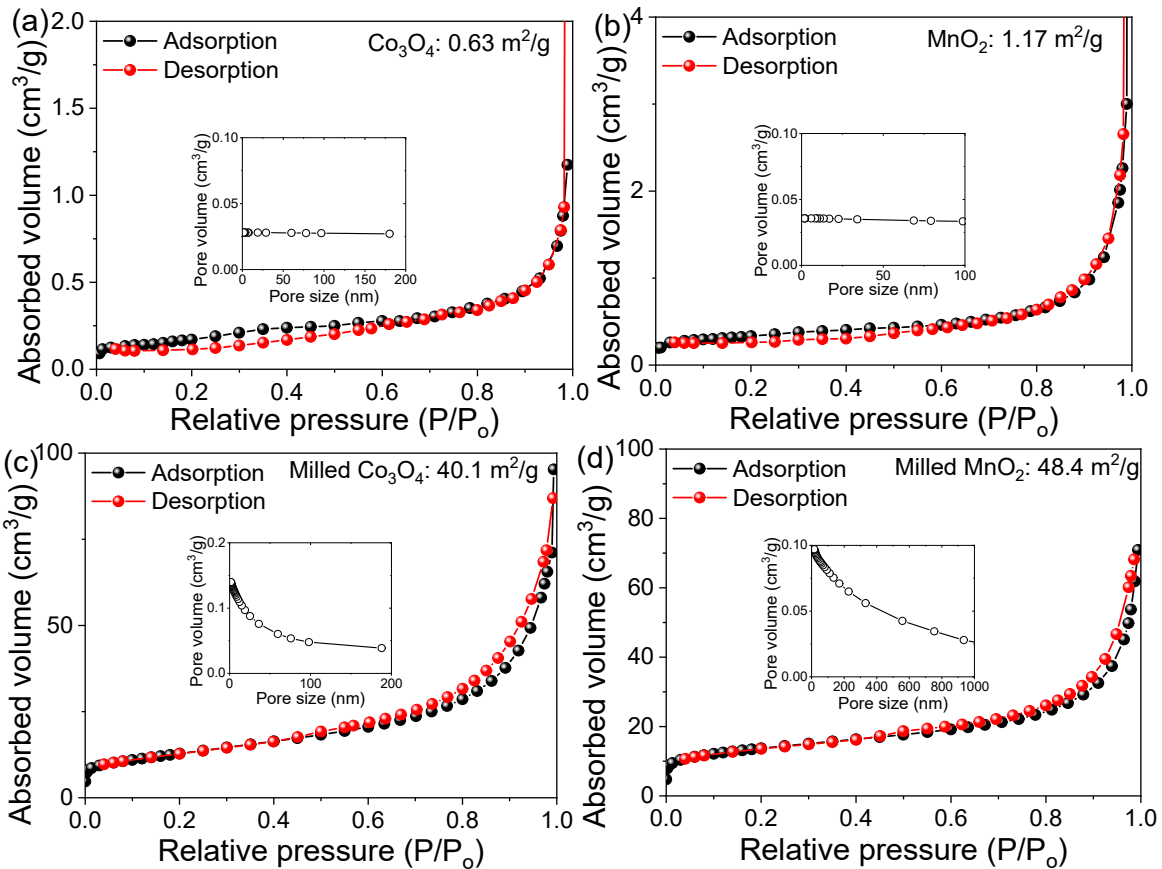
(4)

Figure S4. FE-SEM photos of different magnifications for **(a)** hybridized Co_3O_4/MnO_2; **(b)** Co_3O_4; **(c)** MnO_2; **(d)** milled Co_3O_4; and **(e)** milled MnO_2. (f) Particle size distribution of hybridized Co_3O_4/MnO_2 obtained by SEM image analysis.
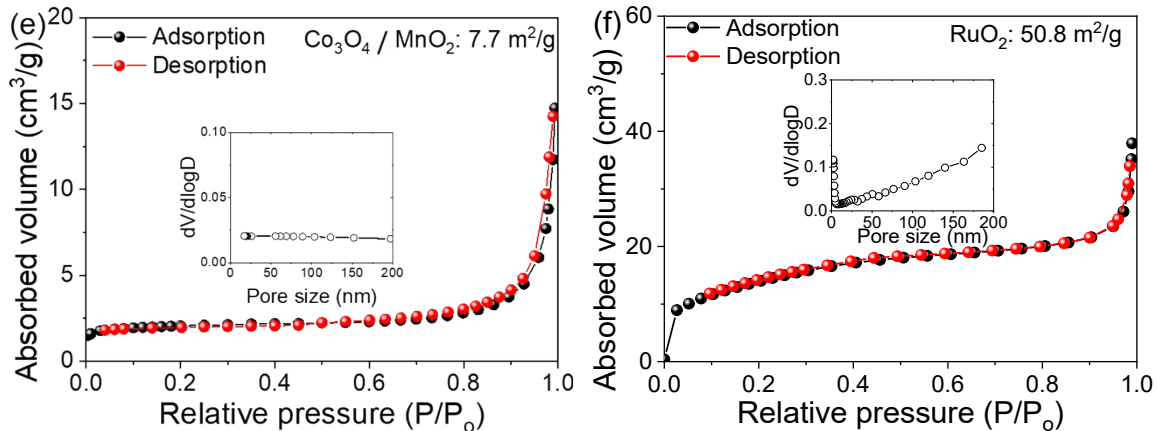
(5)

Figure S5. N$_2$ adsorption/desorption isotherms with the inset Brunauer-Emmett-Teller (BET) surface area and Barrett-Joyner-Halenda (BJH) pore size distribution. We note that Co$_3$O$_4$/MnO$_2$ has a lower BET surface area than that of milled Co$_3$O$_4$ and milled MnO$_2$. This might be attributed to the strong coupling-induced agglomeration. Forming the heterointerface within Co$_3$O$_4$/MnO$_2$ will sacrifice the exposed surface of each oxide, potentially lowering the BET surface area.

(6)
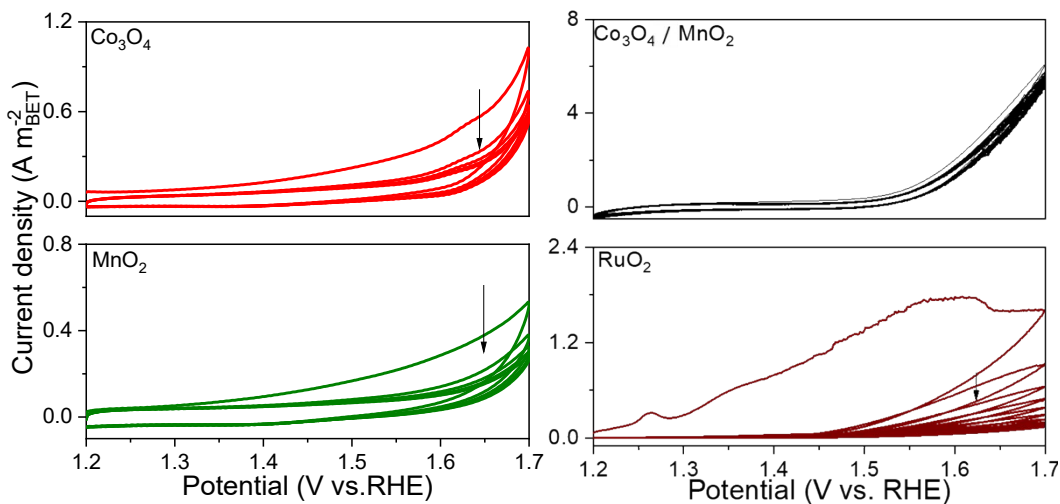
Figure S6. CV curves of Co$_3$O$_4$ (5 cycles), MnO$_2$ (5 cycles), Co$_3$O$_4$/MnO$_2$, and RuO$_2$ (10 cycles)0.5M H$_2$SO$_4$, where the current densities were normalized by the BET surface areas of the metal oxides.

(7)

Figure S7. Linear scan voltammetry of hybridized Co_3O_4/MnO_2 and RuO_2 after 5 cycle pre-CV scans in 0.5M H_2SO_4. The polarization current was normalized by the geometric surface area of the disk electrode.

(8)

The electrochemical active surface area (ECSA) was evaluated using cyclic voltammograms (CVs), which were scanned between 1.1 and 1.2 V vs. RHE. In that potential range, the Faradaic curre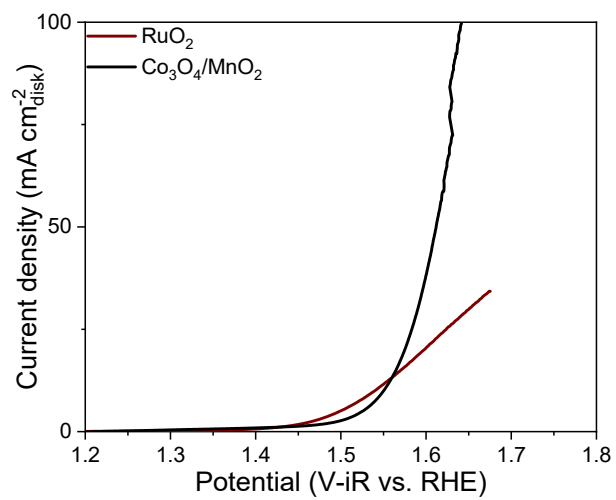nt is negligible and the detected current results from the double-layer capacitive charging. Specifically, the current i depends linearly on the electrochemical double-layer capacitance C_{DL} following: i = $\dot{v} C_{DL}$ where $\dot{v}$ is the potential scan rate (we used 5 mV s^{-1}, 10 m V s^{-1}, 20 mV s^{-1}, and 50 mV s^{-1}). Half of the anodic and cathodic current difference, i.e., $\Delta i/2 = (i_a - i_c)/2$, centered in the middle of the potential scanning range (1.15 V vs. RHE), was used to calculate the capacitance. The ECSA of each sample was calculated by the formula $ECSA = C_{DL}/C_s$, where C_{DL} and C_s represents the double layer capacitance and specific capacitance, respectively. To estimate the ESCA, $C_s =$ 0.1 mF cm^{-2} was applied based on previous reports.[1] No conductive carbon was added when preparing the samples for the above CV scans.
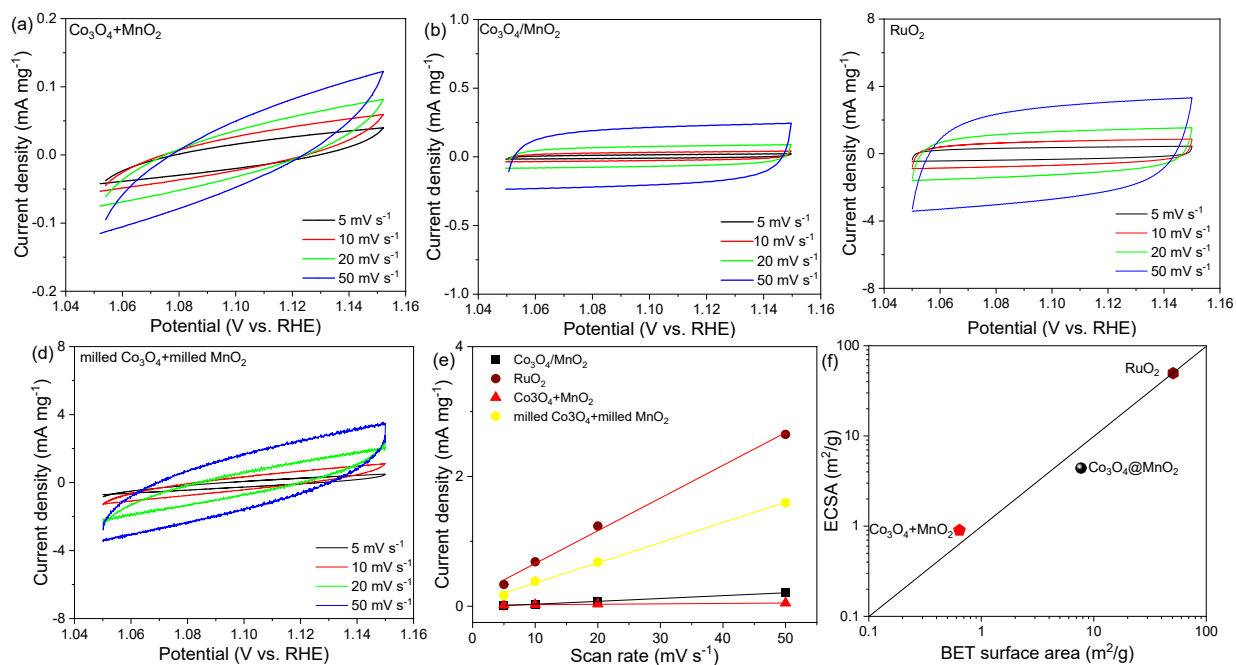
Figure S8. CV curves in the non-faradaic potential region of 1.05-1.15 V vs. RHE for **(a)** Co_3O_4+MnO_2; **(b)** Co_3O_4/MnO_2; **(c)** RuO_2; and **(d)** milled Co_3O_4 + milled MnO_2. **(e)** The capacitive current density as a function of different potential scanning rates. From the slope of Figure **(d)**, the ECSA of Co_3O_4+MnO_2, Co_3O_4/MnO_2, and RuO_2 were determined to be 0.64, 4.4, and 49.6 m^2 g^{-1}, respectively. **(e)** The comparison between the BET surface area and the ECSA. The order of ECSA results generally matched that of their BET surface areas, a trend consistent with previous benchmarking study (J. Mater. Chem. A, 2016, 4, 3068-3076).
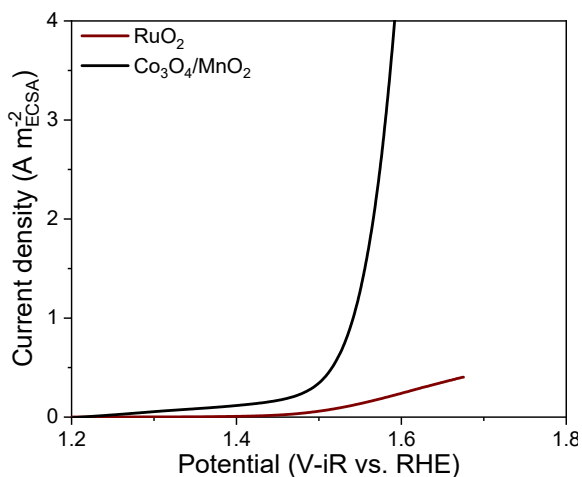
(9)

Figure S9. Comparison of normalized OER current density by the ECSA. Linear scan voltammetry was measured after 5 cycles of pre-CV scans in 0.5M H_2SO_4. We noted that RuO_2 has a geometric activity inferior to that of Co_3O_4/MnO_2 at large OER potentials (Figure S7), but larger ECSA (Figure S8), leading to a lower specific OER activity as presented in this plot.

(10)
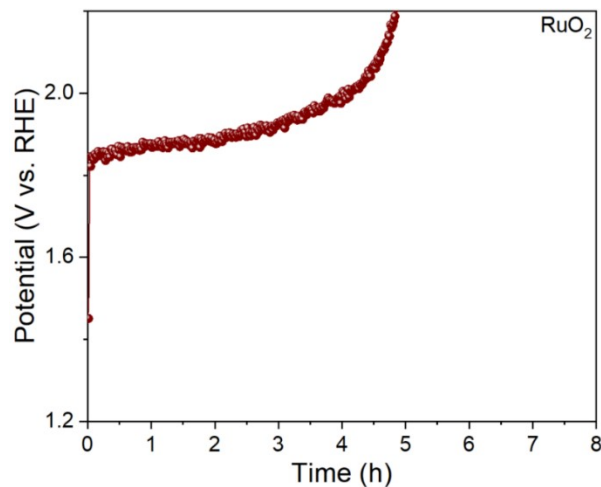
Figure S10. Chronopotentiometry test of RuO_2 at the current density of 100 mA cm^{-2} in 0.5M H_2SO_4. RuO_2 was loaded on a Ti felt for the test and the current density was normalized by the geometric surface area of the Ti felt.

(11)
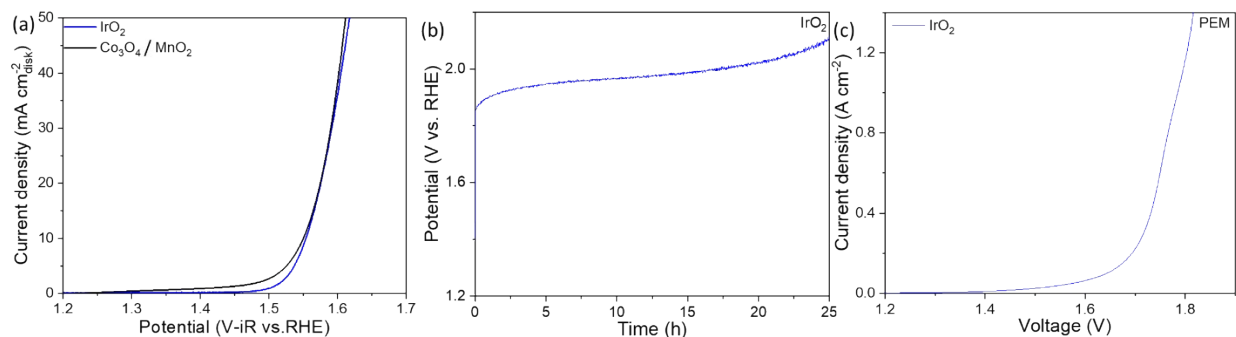
Figure S11. (a) Linear scan voltammetry of hybridized Co_3O_4/MnO_2 and IrO_2 in 0.5M H_2SO_4. (b) Chronopotentiometry test of IrO_2 at the current density of 100 mA cm^{-2} in 0.5M H_2SO_4. **(c)**

Polarization curve of a PEMWE cell at 80 °C with IrO$_2$ as the anode and Pt/C as the cathode. The voltage was iR-corrected.

(12)
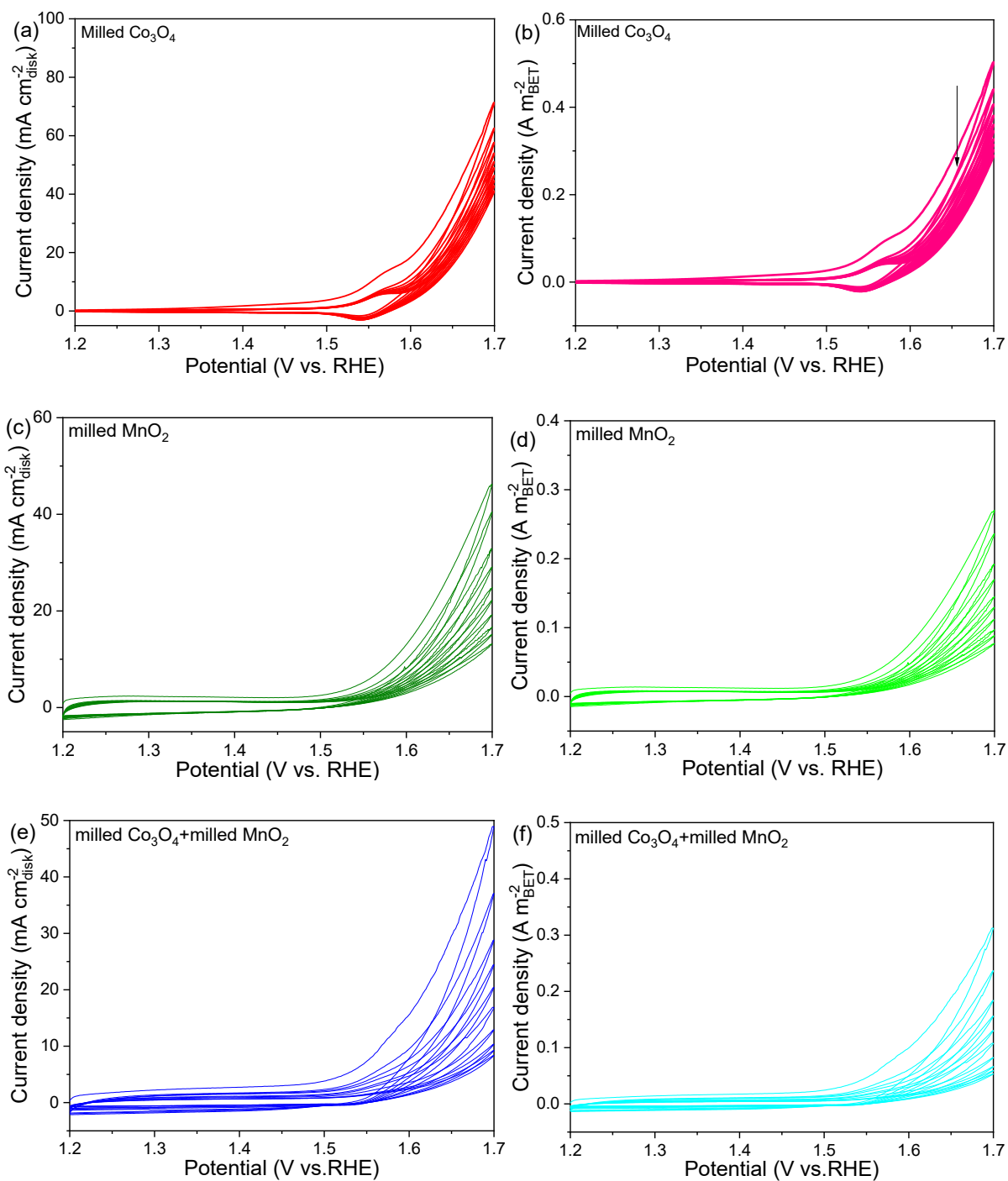
Figure S12. CV curves of studied catalysts in 0.5M H_2SO_4: **(a)** and **(b)** milled Co_3O_4; **(c)** and **(d)** milled MnO_2; **(e)** and **(f)** milled Co_3O_4+milled MnO_2, where polarization current densities were normalized by the glassy carbon disk area and the BET area of metal oxides.

(13)
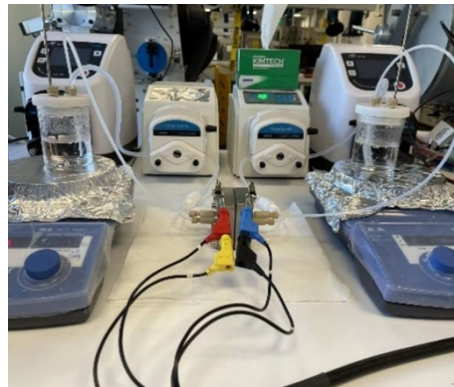
Figure S13. Home-made testing setup of PEMWE cell.

(14)
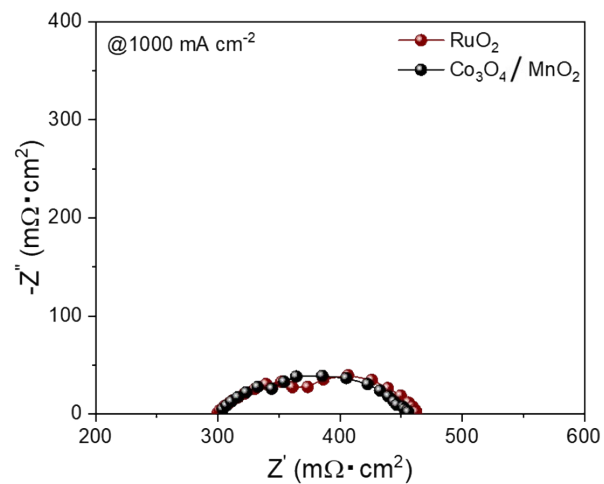
Figure S14. EIS of the PEMWE cell with studied catalysts as the anode,. The polarization resistance was calculated as the distance between the two points of the impedance intersecting the real axis of the Nyquist plot.

(15)
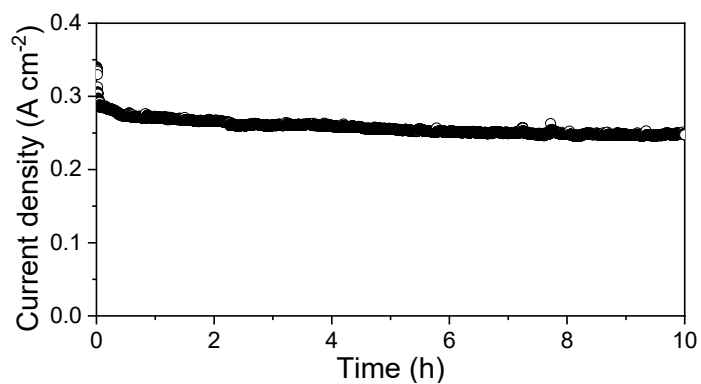
Figure S15. Chronoamperometry test of a PEMWE cell with the Co_3O_4/MnO_2 as the anode at a voltage of 1.7 V.

(16)
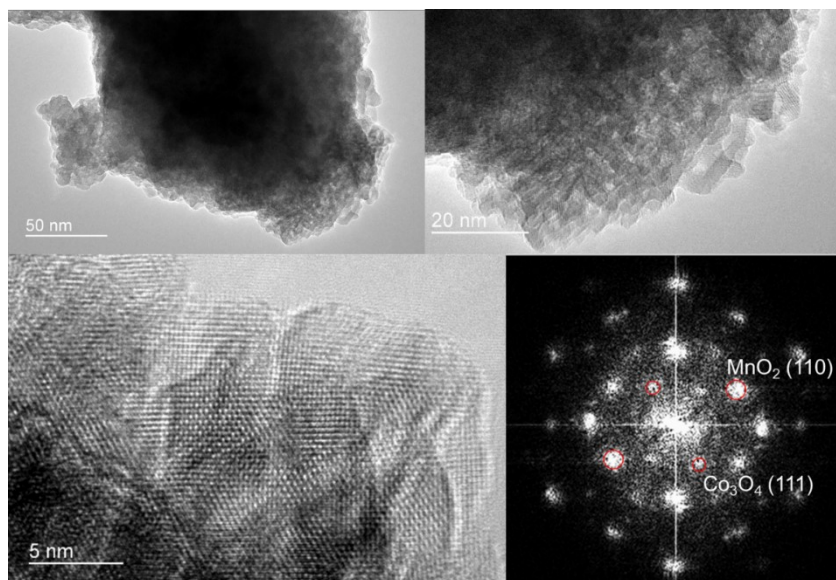
Figure S16. TEM of hybridized Co_3O_4/MnO_2 with the corresponding FFT.

(17)
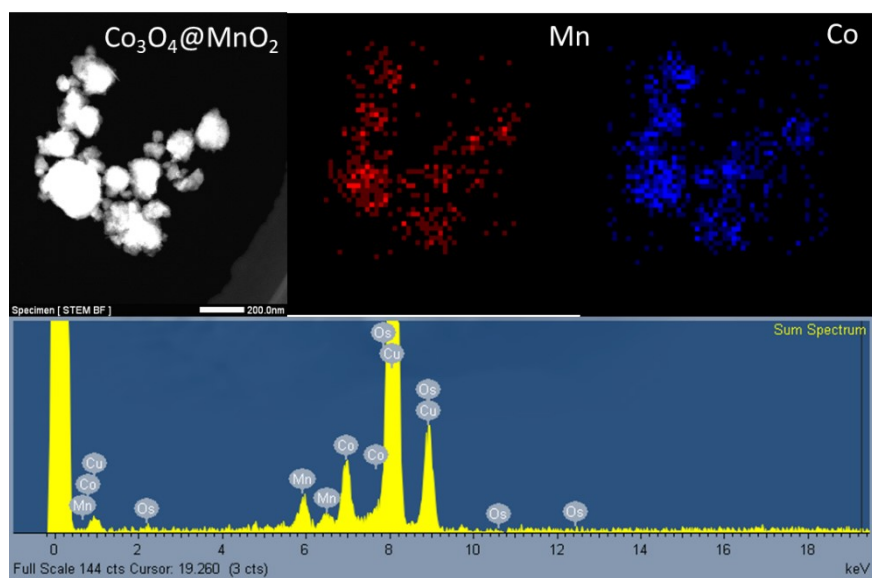
Figure S17. HAADF-STEM image and EDS mapping with sum spectrum of hybridized Co_3O_4/MnO_2.

(18)

(a) Co 2p
Co₃O₄/MnO
Co₃O₄

(b) Mn 2p
Co₃O₄/MnO
MnO

(c) Co 2p
Co₃O₄/Mn₃O₄
Co₃O₄

(d) Mn 2p
Co₃O₄/Mn₃O₄
Mn₃O₄
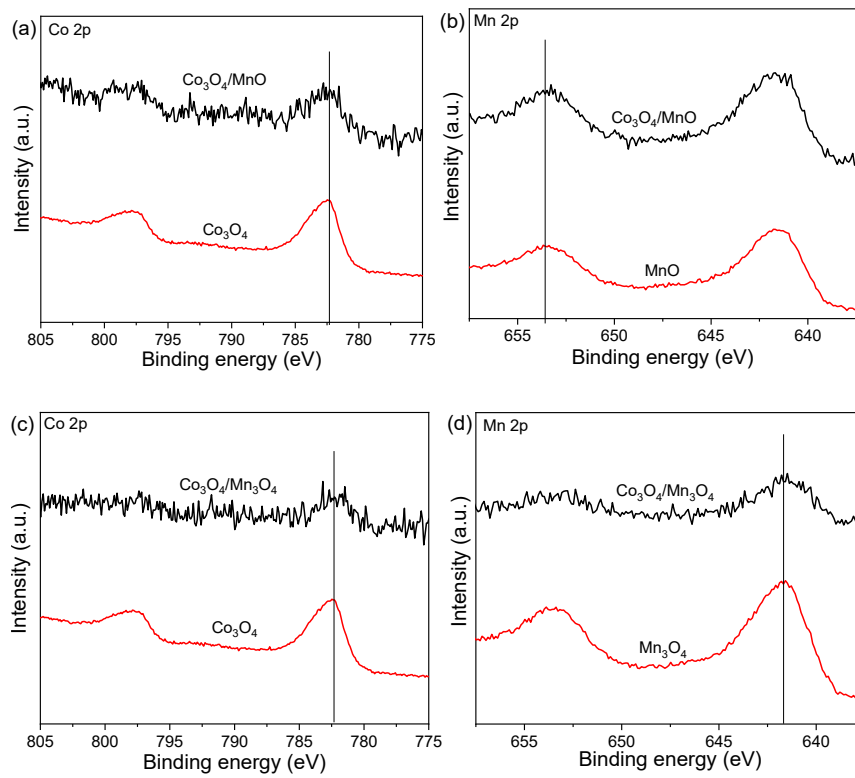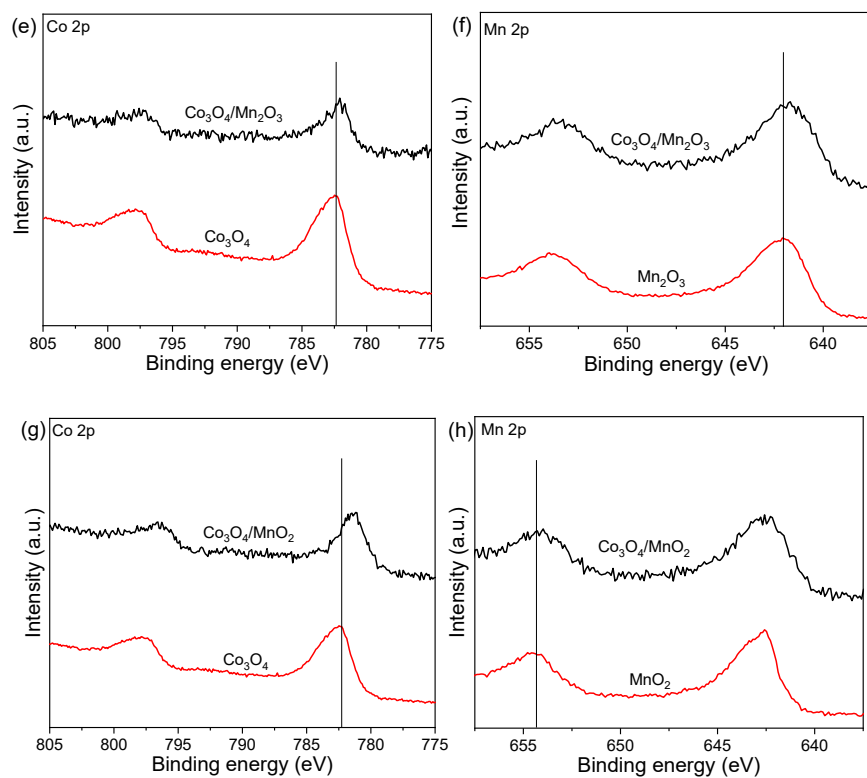
Figure S18. Co 2p and Mn 2p XPS for hybridized Co_3O_4/MoO_x.

(19)
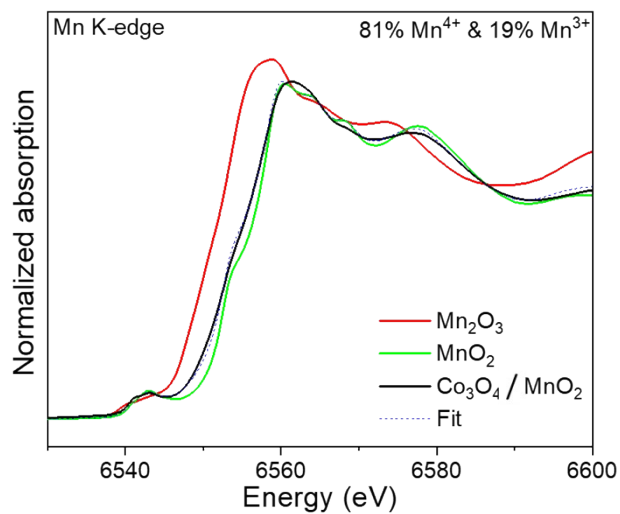
Figure S19. Linear combination fitting of Mn K-edge XANES for Co_3O_4/MnO_2 with Mn_2O_3 and MnO_2 as the standards.

(20)
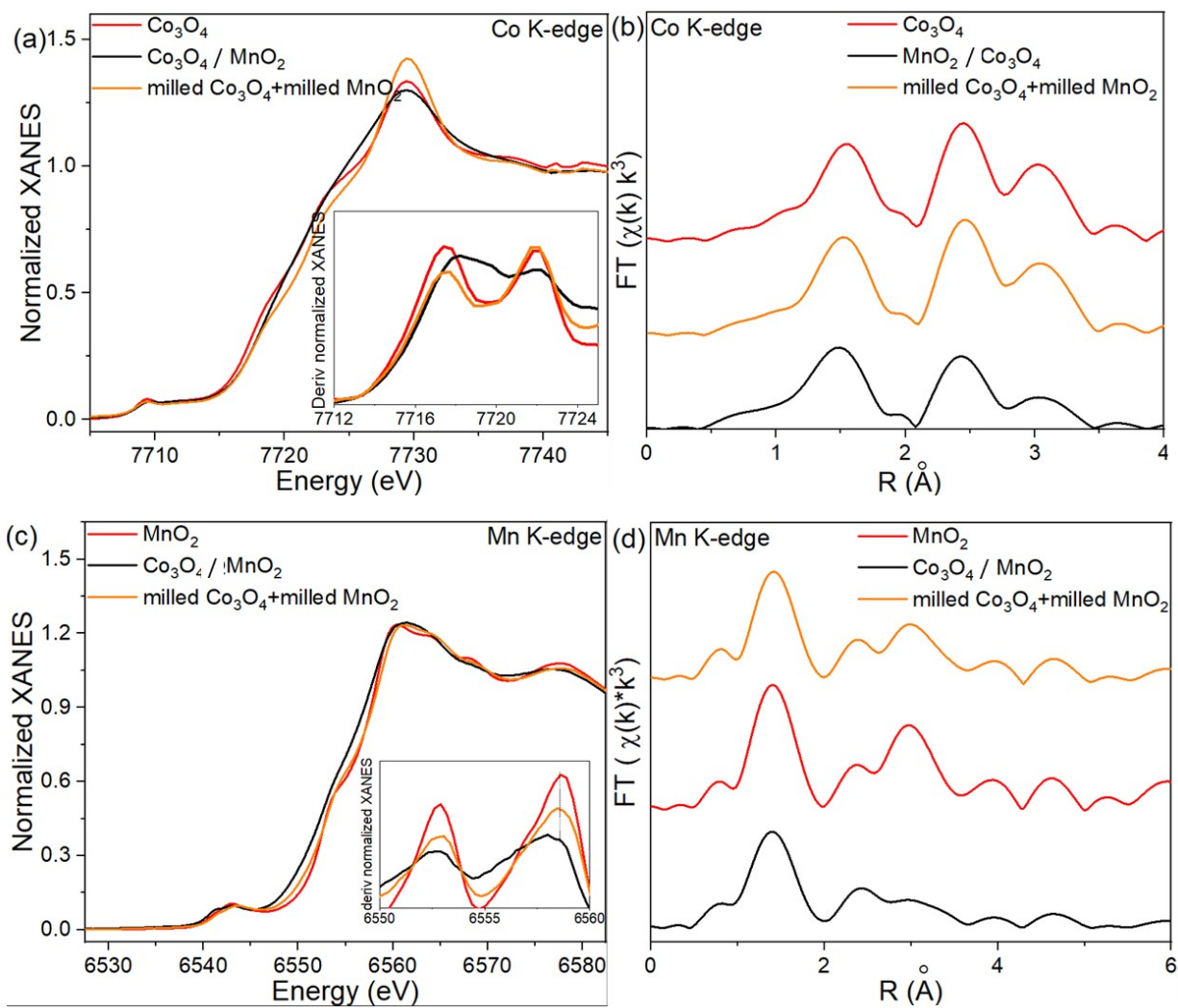
Figure S20. Co K-edge and Mn K-edge XAFS of milled Co_3O_4 mixed simply with milled MnO_2 (milled Co_3O_4+milled MnO_2).

(21)
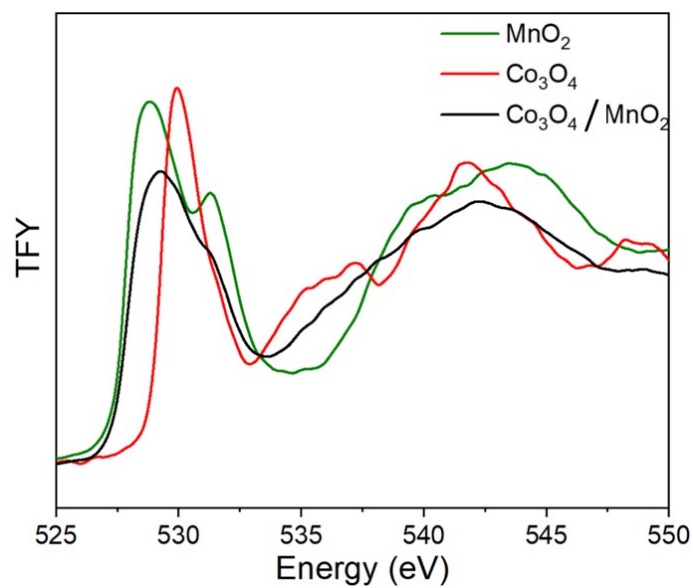
Figure S21. O K-edge TFY sXAS of Co_3O_4, MnO_2, and Co_3O_4/MnO_2.

(22) By comparing the Non-normalized XAFS profiles, we found that the intensity of the white line in the non-hybridized sample ($Co_3O_4+MnO_2$) was reduced after polarization compared to its

intensity at OCV, which might reflect some components of the sample experienced leaching.[2] In contrast, the hybridized sample (Co_3O_4/MnO_2) exhibited no significant changes in the XAFS white line intensity after polarization, suggesting that it may be more resistant to leaching.
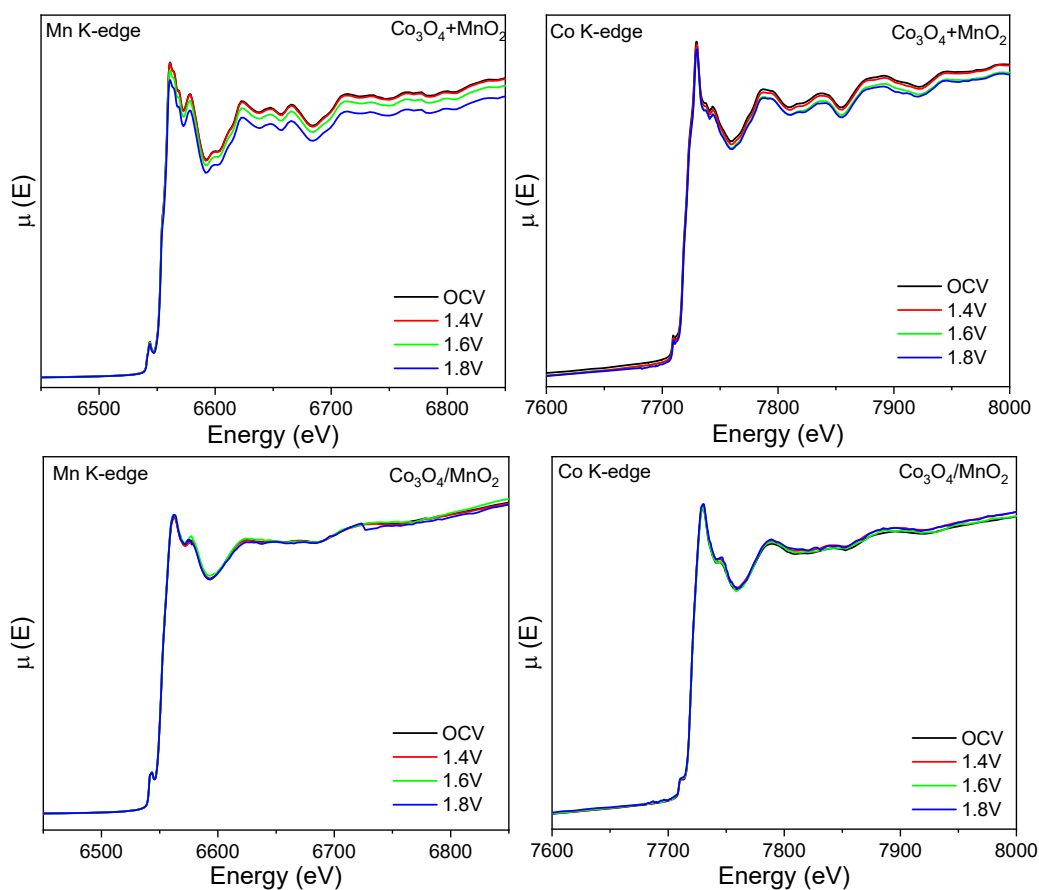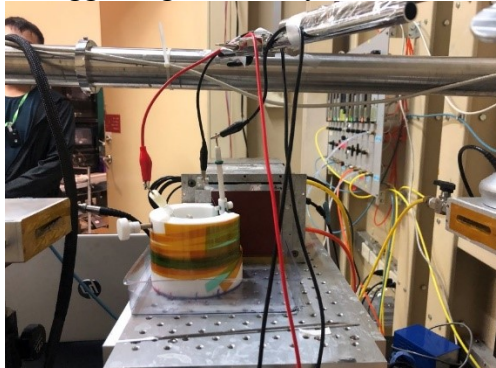
Figure S22. (a) Photograph of the experimental setup for the operando XAFS test, **(b)-(e)**

Non-normalized in-situ XAFS spectra around the cobalt K-edge and Mn K-edge.

(23)
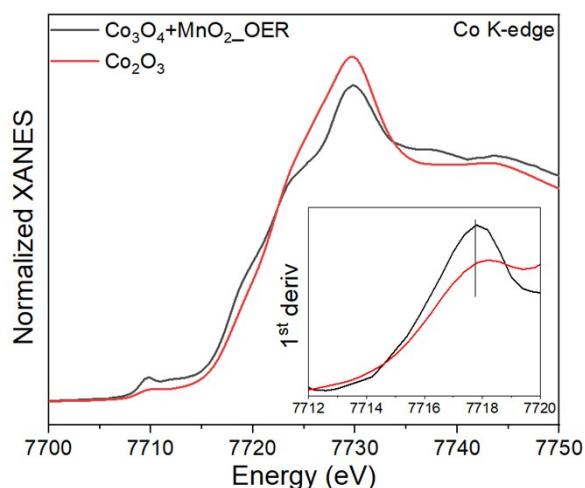
Figure S23. Co K-edge XANES of OER-polarized $Co_3O_4+MnO_2$ as compared with that of Co_2O_3.

The Co K-edge energy of OER-polarized $Co_3O_4+MnO_2$ was lower than that of Co_2O_3 from the 1st

derivative of normalized XANES, indicating a valence lower than +3.

(24)
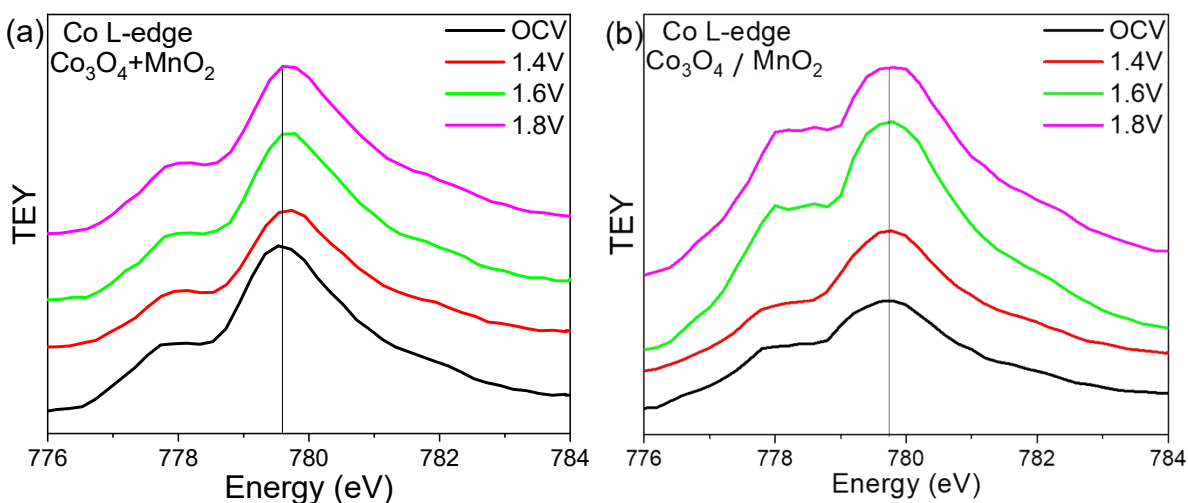
Figure S24. Co L-edge TEY at different potentials for **(a)** simply-mixed $Co_3O_4+MnO_2$ and **(b)**

hybridized Co_3O_4/MnO_2. Compared with the OCV state, Co L-edge sXAS of $Co_3O_4+MnO_2$ moved

positively by ~0.3 eV at 1.8V vs. RHE, suggesting Co oxidation. In contrast, Co L-edge sXAS of

Co_3O_4/MnO_2 remained almost no shift.

(25)
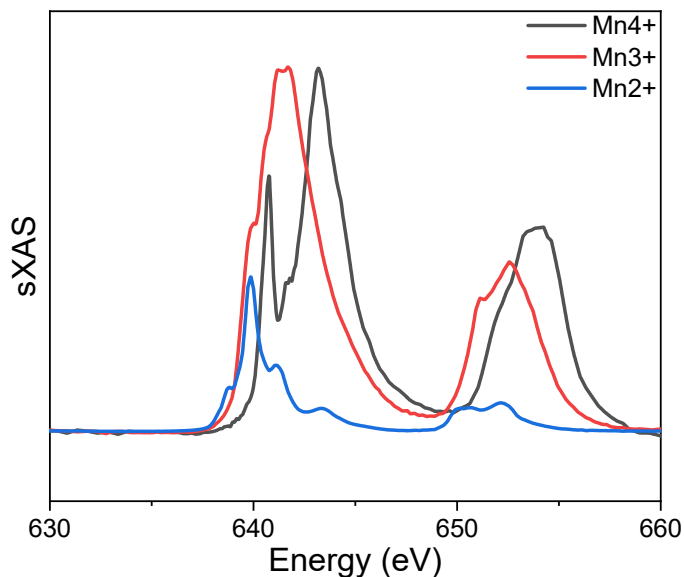
Figure S25. Mn L-edge sXAS of standard Mn^{4+}, Mn^{3+}, and Mn^{2+}, where MnO_2, Mn_2O_3, and MnO were used as the reference samples to measure the standard spectrum.

(26)
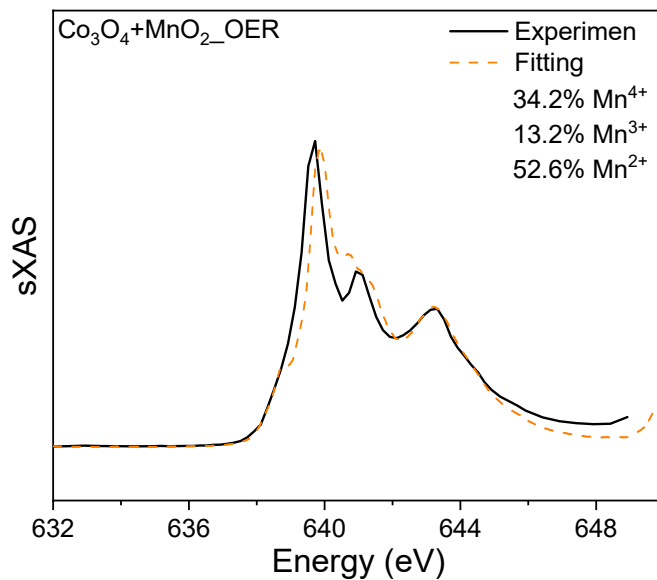
Figure S26. Linear combination fitting of Mn L-edge sXAS for OER-polarized $Co_3O_4+MnO_2$. The fitting error was ~ 4.8%.

(27)
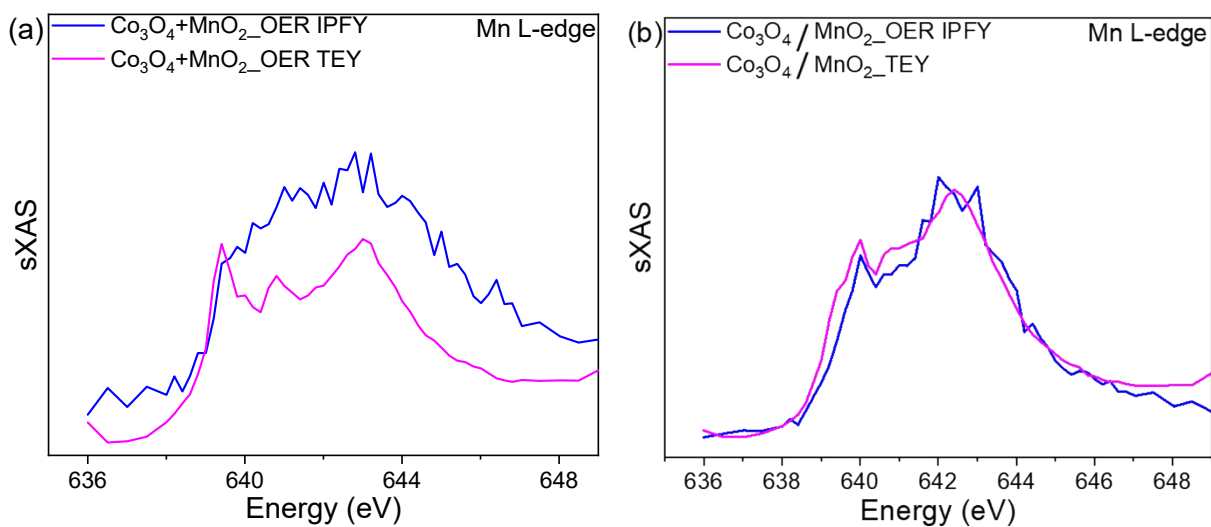
Figure S27. RIXS-sXAS in TEY and IPFY modes around Mn L-edge for OER-polarized **(a)** $Co_3O_4+MnO_2$ and **(b)** Co_3O_4/MnO_2.

(28)
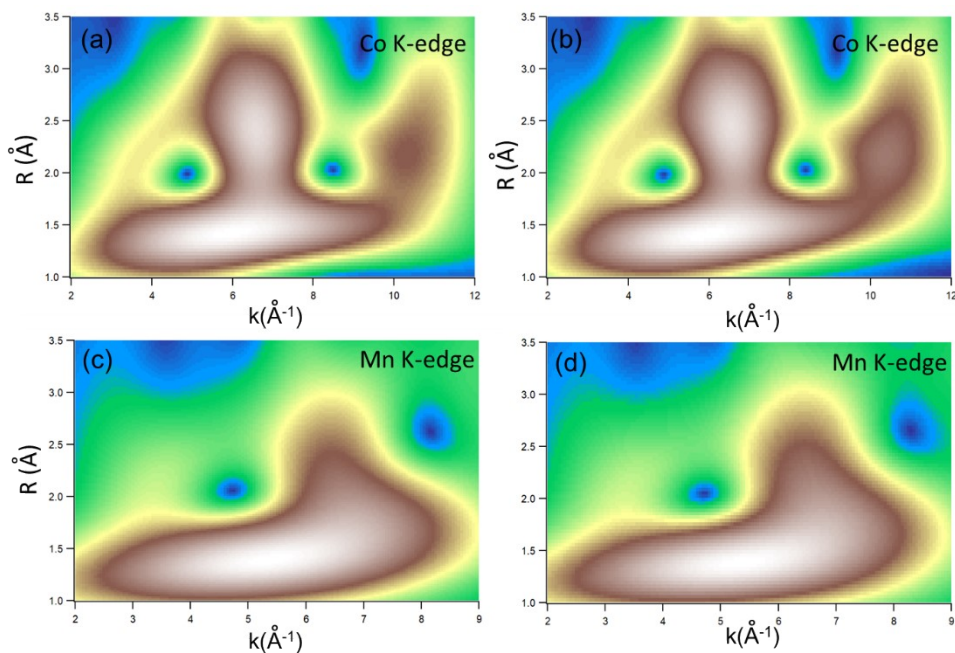
Figure S28. Co K- and Mn K-edge WT-EXAFS of Co_3O_4/MnO_2 before (**(a)** and **(c)**) and after (**(b)** and **(d)**) the OER polarization.
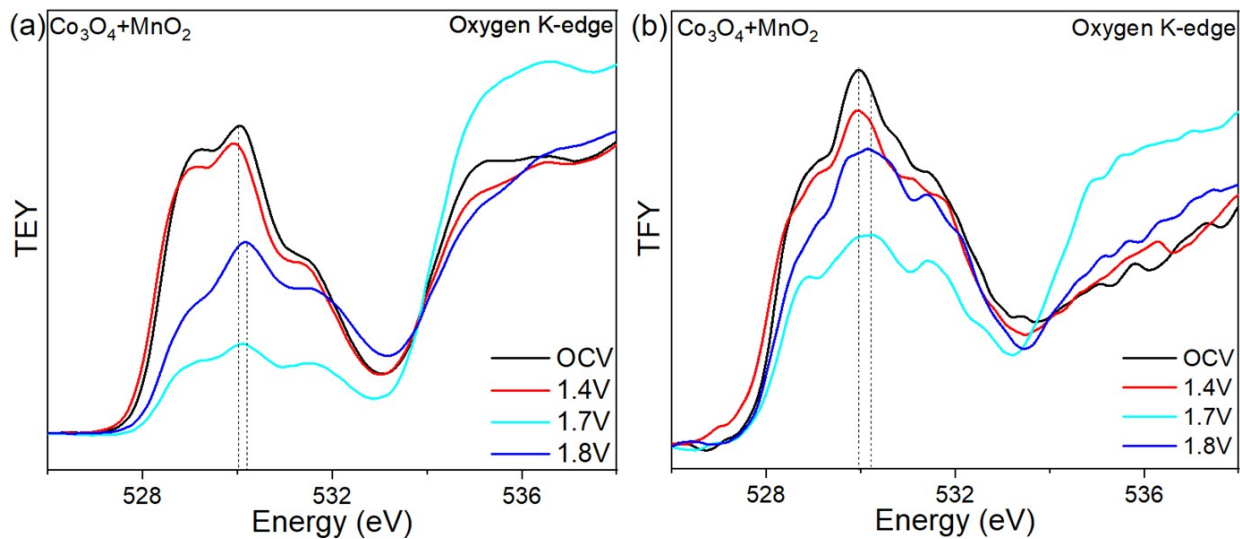
Figure S29. O K-edge **(a)** TEY and **(b)** TFY sXAS of Co_3O_4+MnO_2 at different potentials. Compared with the OCV state, sXAS shifted negatively by ~0.1 eV at 1.4V, and positively by ~0.2 eV at 1.7 and 1.8 V. The voltage refers to RHE.

(30)
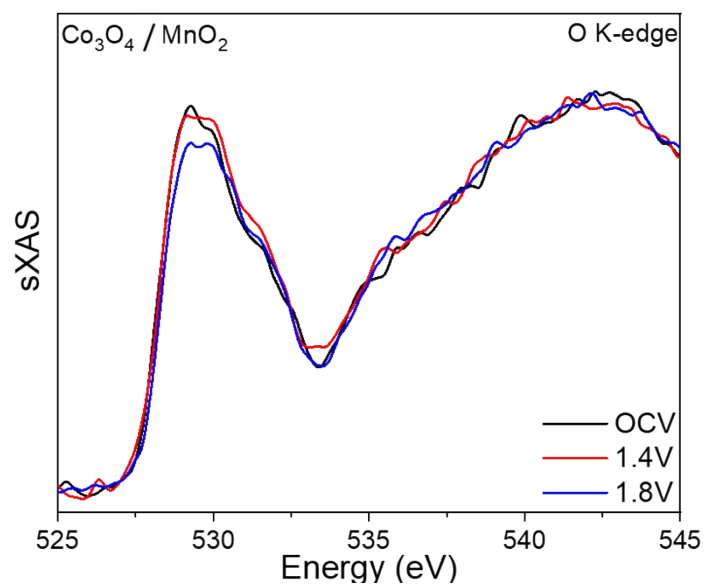
Figure S30. O K-edge sXAS of OER-polarized Co_3O_4/MnO_2 at different potentials.

(31)
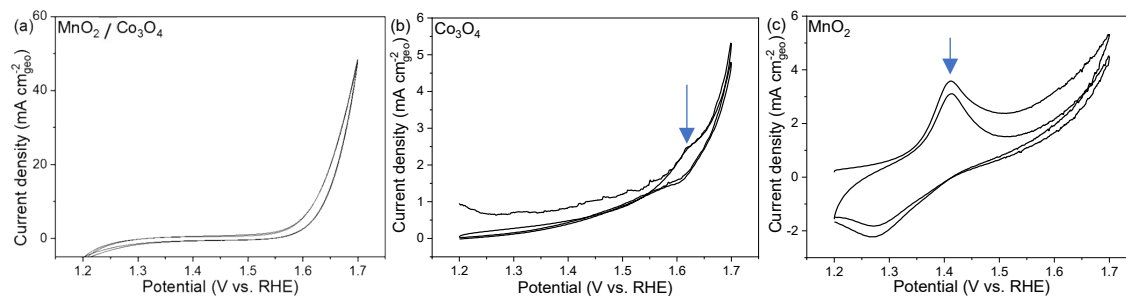
Figure S31. Initial two CV curves in 0.5 M H_2SO_4, where the metal oxide was loaded on carbon paper for the measurement and the current density was normalized by the geometric surface area of the carbon paper.

(32)
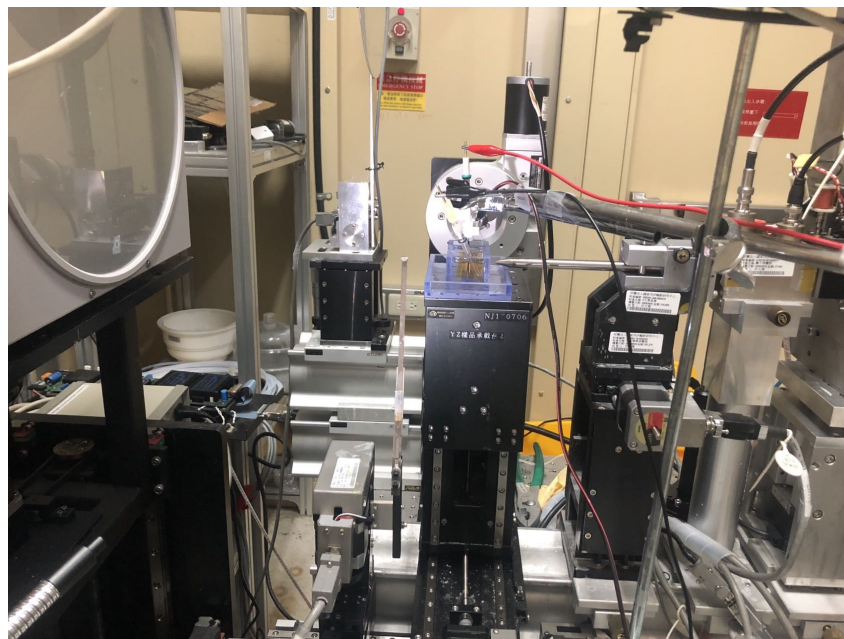
Figure S32. Photograph of the experimental setup for the operando XRD test in 0.5M H_2SO_4.

(33)
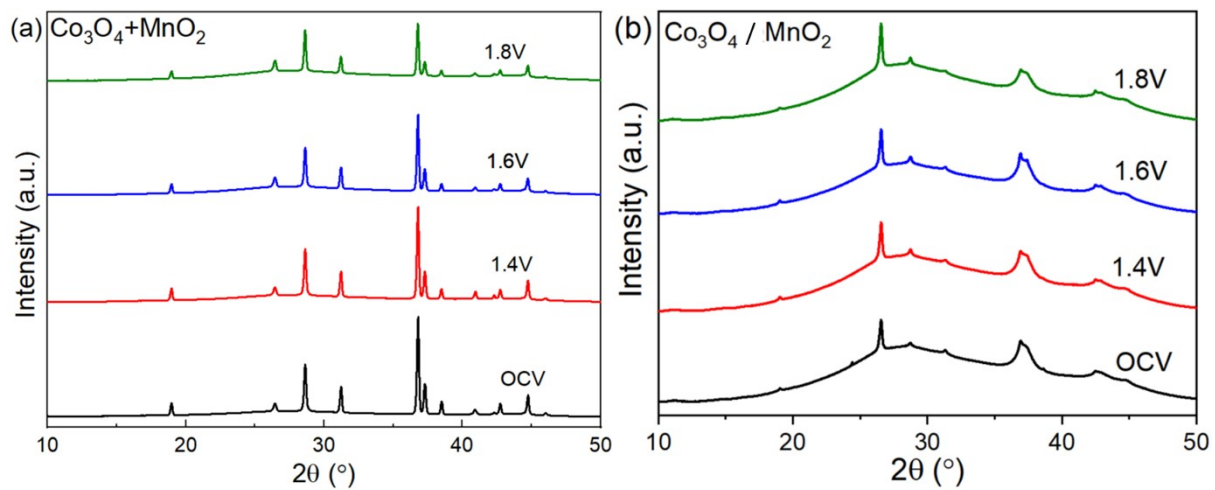
Figure S33. In-situ XRD pattern of (a) $Co_3O_4+MnO_2$ and (b) Co_3O_4/MnO_2 at different potentials.

The diffraction peak around 26° is indexed to the carbon paper.

(34)
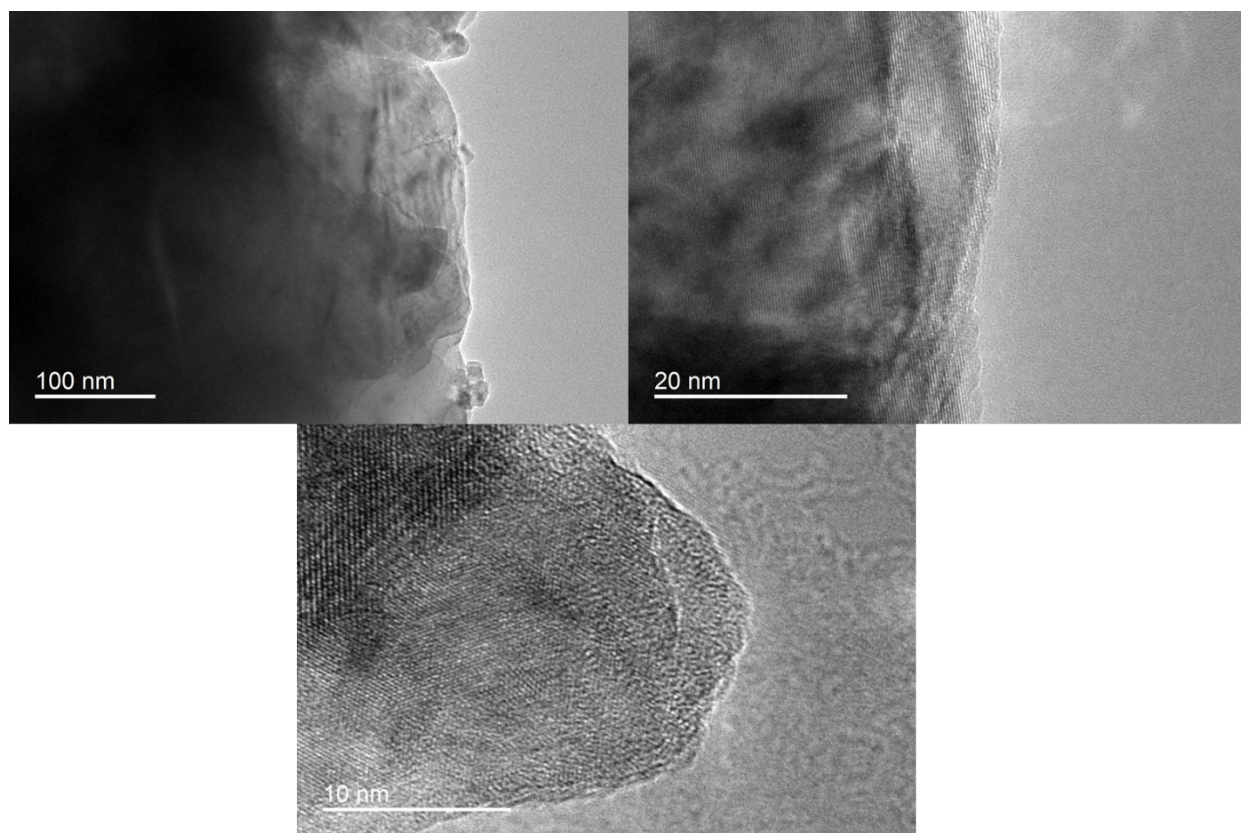
Figure S34. TEM of different magnifications for Co_3O_4 after the OER polarization in 0.5M H_2SO_4.

(35)
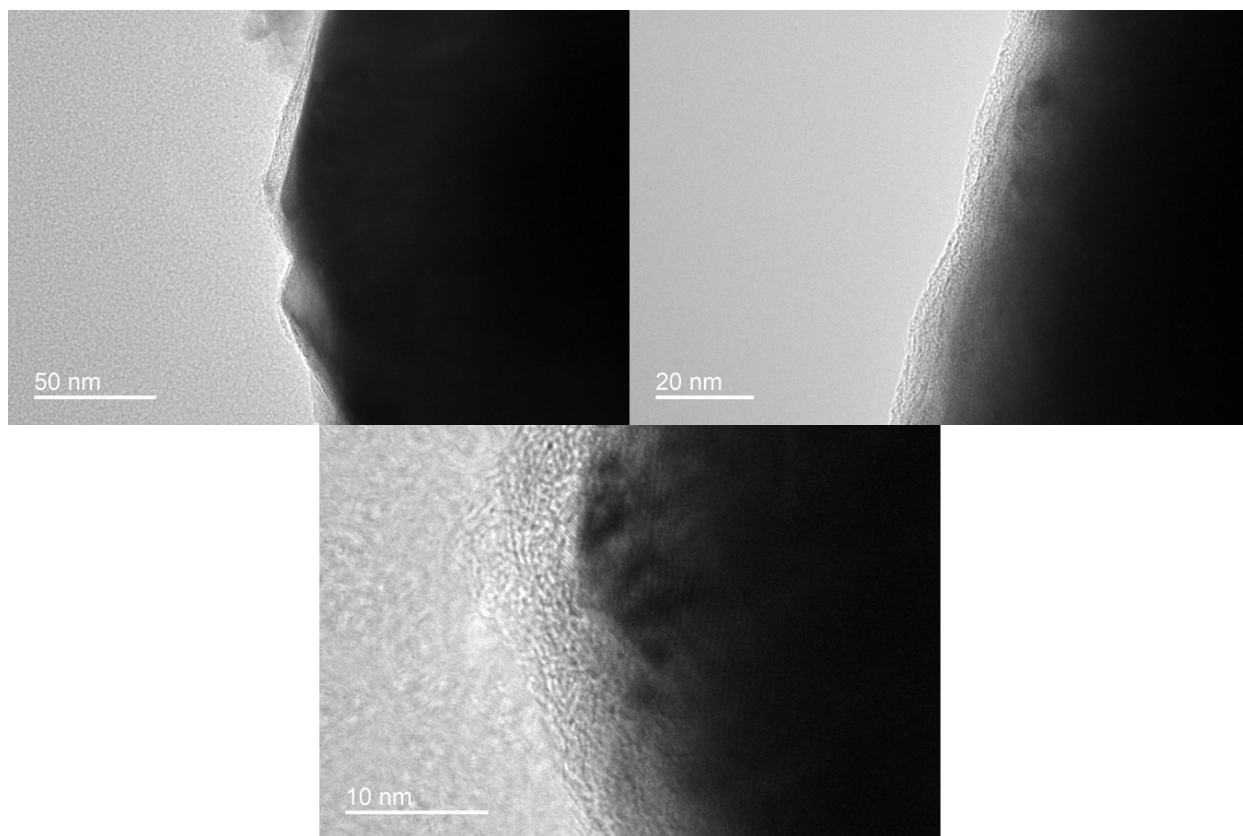
Figure S35. TEM of different magnifications for MnO_2 after the OER polarization in 0.5M H_2SO_4.

(36)
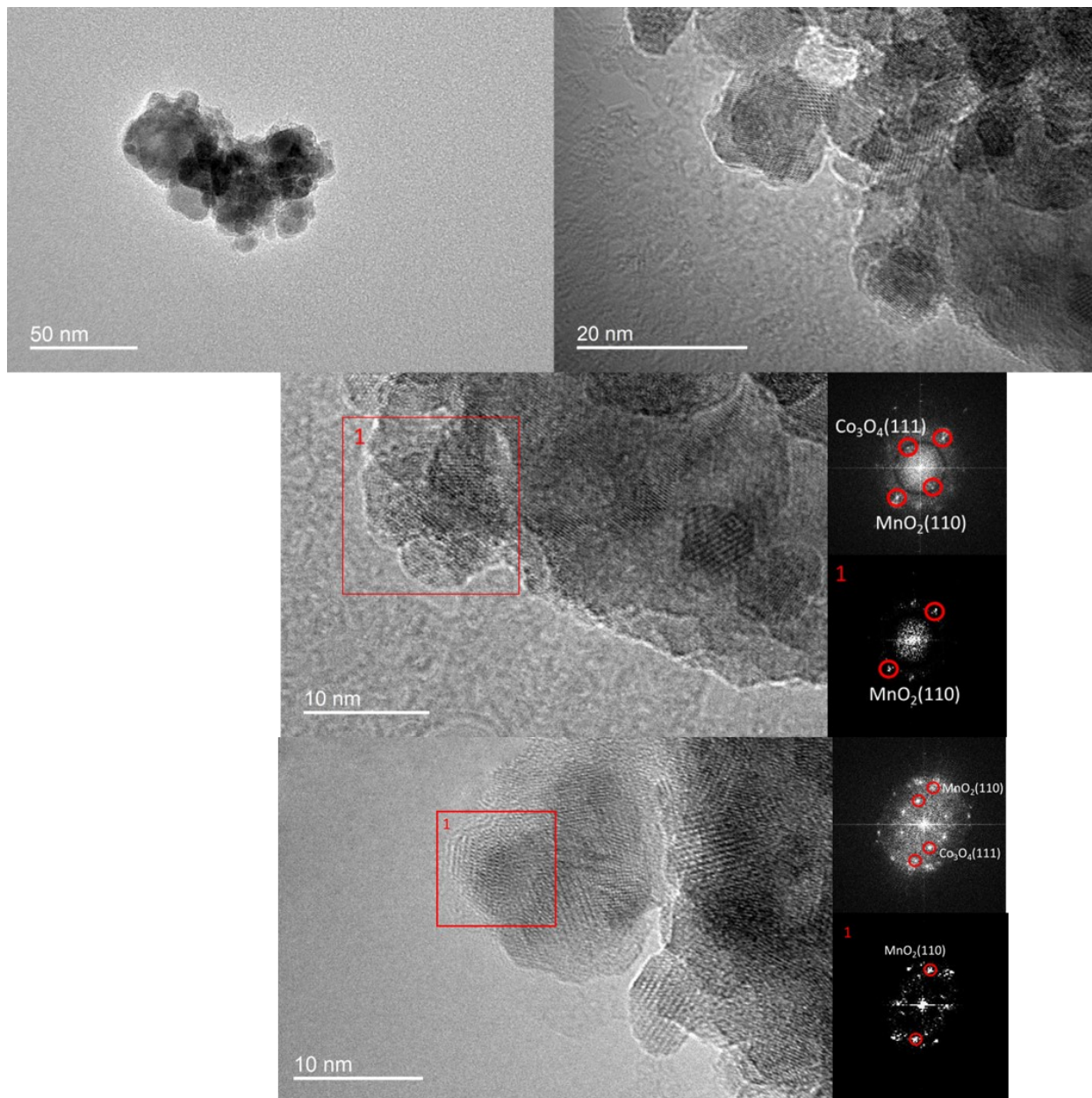
Figure S36. TEM of different magnifications for Co_3O_4/MnO_2 after the OER polarization in 0.5M H_2SO_4. The above FFT represents the whole image region, while the below FFT corresponds to the red-color region.

(37)
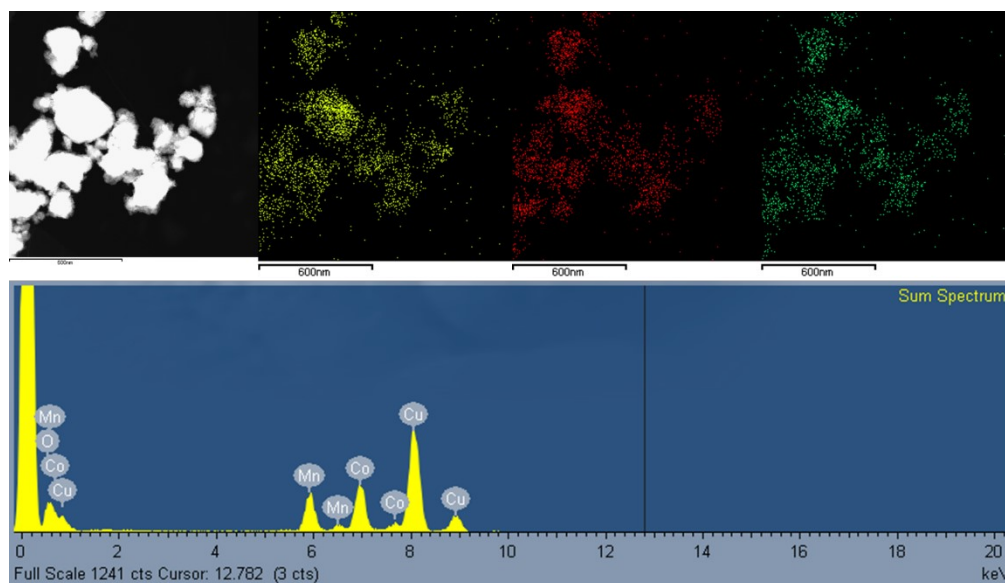
Figure S37. HAADF-STEM image and EDS mapping with sum spectrum of OER-polarized Co_3O_4/MnO_2. The yellow, red, and green colors correspond to Co, Mn, and O element, respectively.

(38)
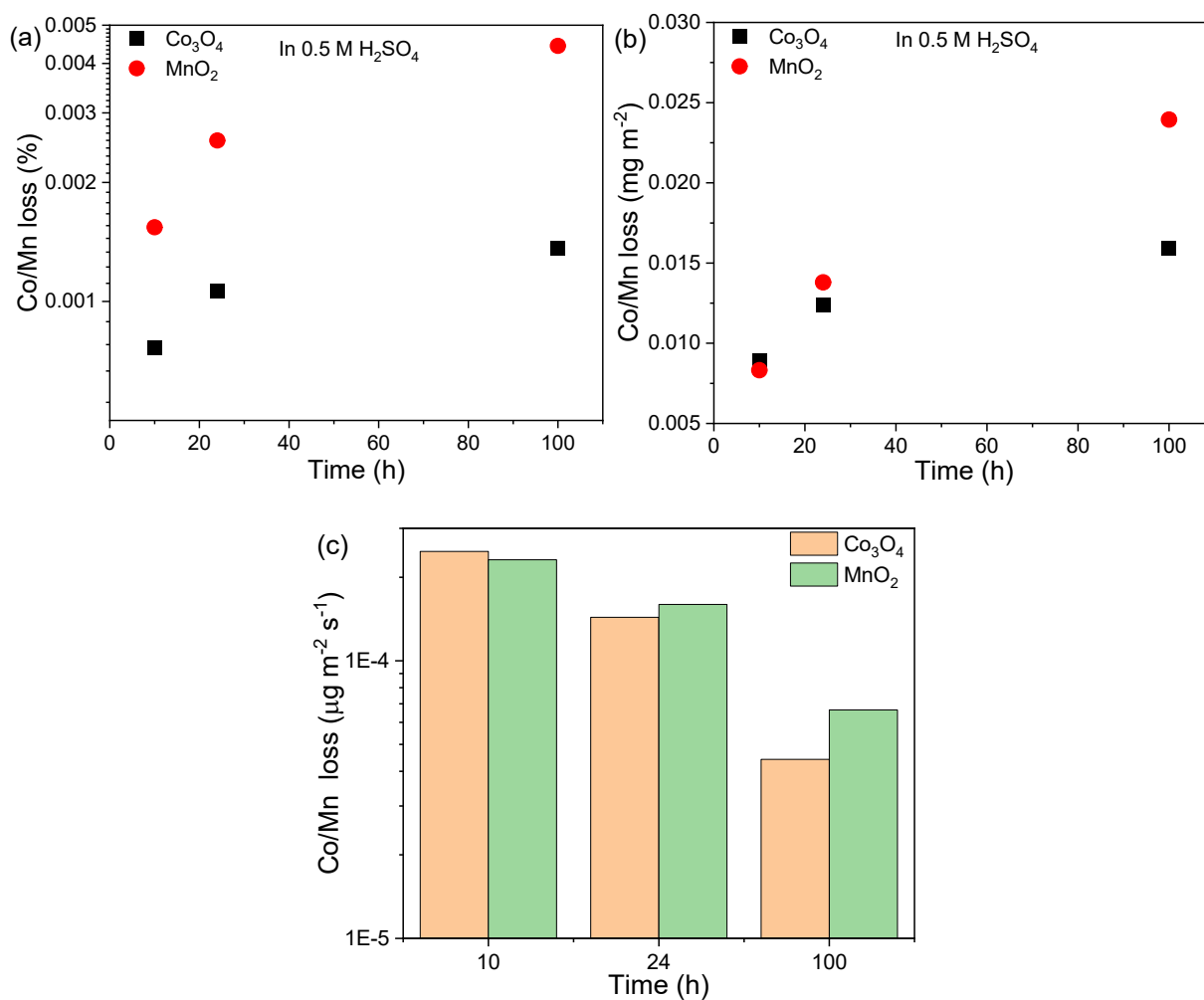
Figure S38. ICP-MS-detected dissolution of Mn and Co after soaking MnO_2 and Co_3O_4 individually in 0.5 M H_2SO_4 for different time: **(a)** relative loss in percentage; **(b)** mass loss per unit BET surface area of MnO_2 and Co_3O_4; **(c)** average dissolution rate per unit BET surface area

of MnO_2 and Co_3O_4. From **Figure (c)**, we note that the average dissolution rate decreased with time, suggesting the gradually stabilized leaching, which might be attributed to the balance of dissolution and redeposition of leached cations.

(39)
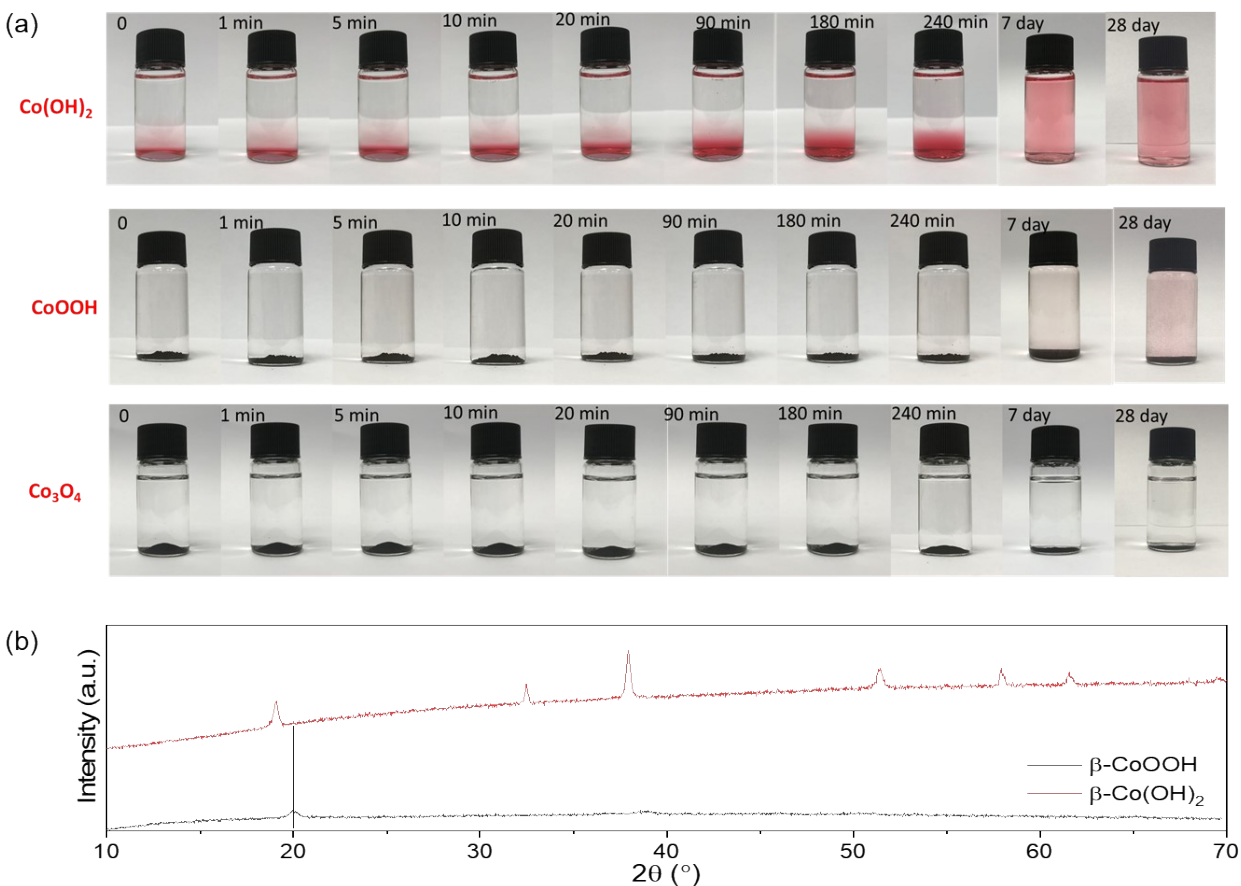
Figure S39. (a) Photo of $Co(OH)_2$, CoOOH, and Co_3O_4 soaked in 0.5 M H_2SO_4 for different lengths of periods. $Co(OH)_2$ was received from Aladdin without additional treatment. CoOOH was made by stirring the mixture of $Co(OH)_2$ with NaClO in 1 M KOH for 24 hours.[3] Their XRD patterns in **(b)** are well indexed into those of β-Co(OH)2 and β-CoOOH. For $Co(OH)_2$, it was dissolved rapidly turning the solution color pink. The crystalline CoOOH was also partially

dissolved, as reflected by the gradual color change of the solution. Co_3O_4 exhibited a much stronger corrosion resistance, without obviously being dissolved.

(40)
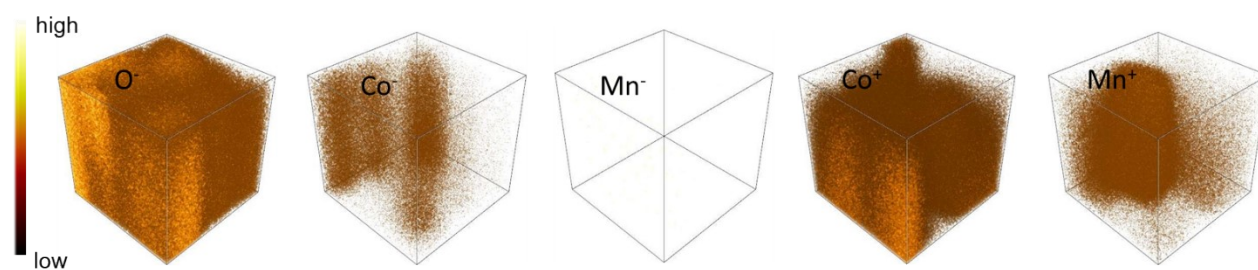
Figure S40. TOF-SIMS-derived 3D images of postive and negative ions for Co_3O_4/MnO_2 after OER cycling in 0.5M H_2SO_4.

(41)
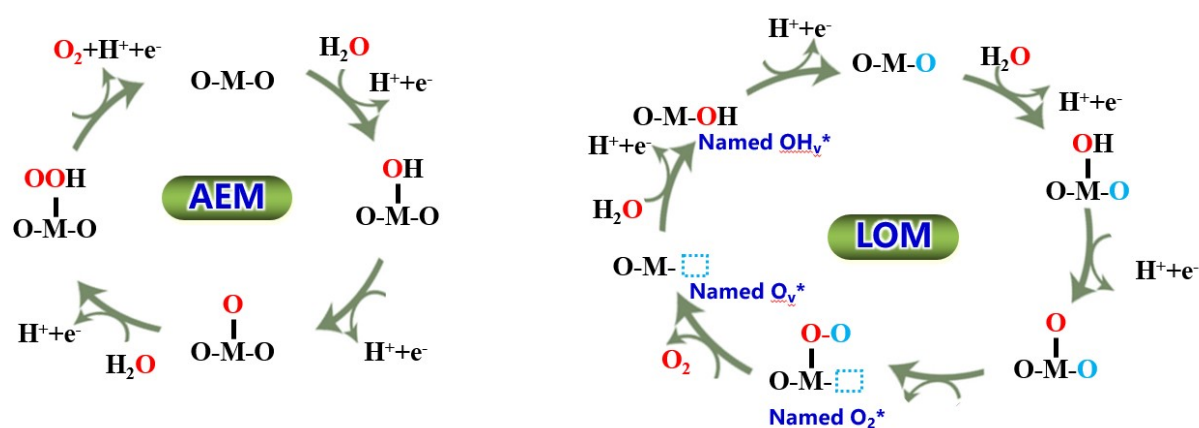
Figure S41. Elemental steps for the OER process following the AEM and LOM pathway.

(42)
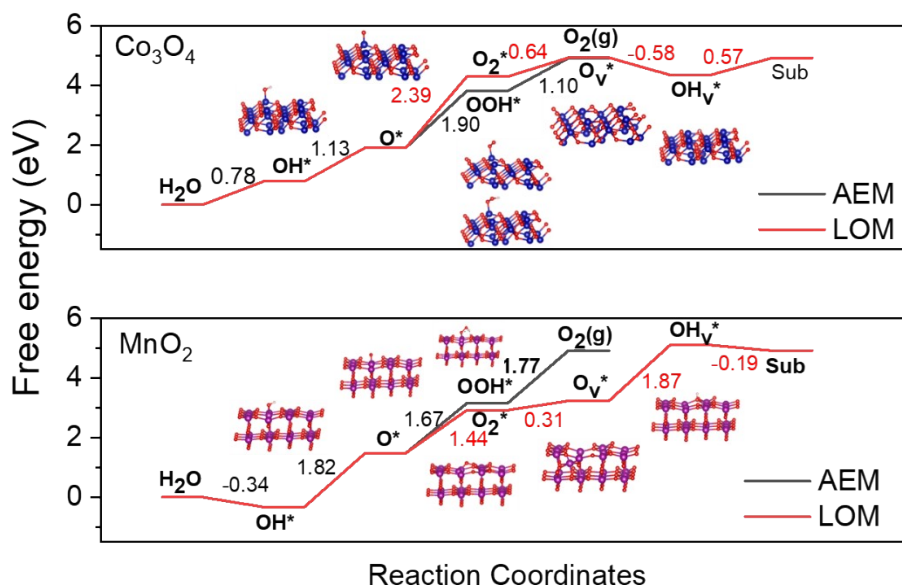
Figure S42. Free energy diagram of elemental steps at U = 0 V for $Co_3O_4(111)$ and $MnO_2(110)$ based on the AEM and LOM processes.

(43)

From the results shown below, for the -O binding (magenta color curve), the PDOS was more obviously uplifted relative to the Fermi level on Mn site compared to that on Co site, consisting with the stronger O adsorption on Mn site as shown in Figure 4a. In contrast, the PDOS change was less significant for OOH adsorption on both Co and Mn sites in Co_3O_4/MnO_2 (blue color curve relative to green color curve), indicating a similar OOH adsorption strength. This result was consistent with our analysis of free energy diagram of OER elemental steps (Figure 4a): in Co_3O_4/MnO_2, Co site with weaker O adsorption contributed to a lower theoretical OER overpotential than Mn site.
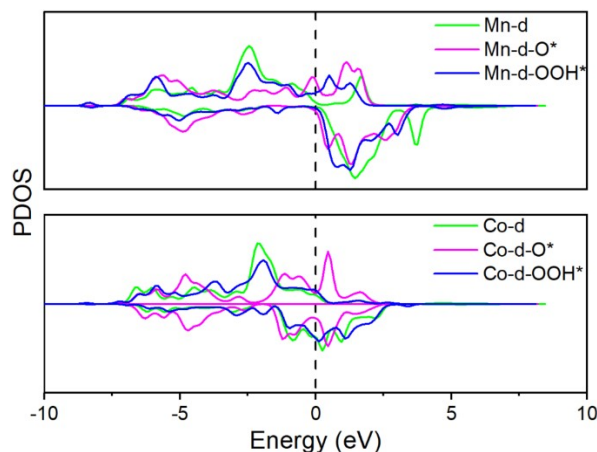
Figure S43. Computed partial density of states (PDOS) of Co-*d* orbital and Mn-*d* orbital in Co_3O_4/MnO_2 for substrates, O*, and OOH*.

(44)

The thermodynamic stability of Co_3O_4/MnO_2 was characterized by surface Pourbaix diagram, which was constructed by the stable surface at the relevant U_{SHE} (standard hydrogen electrode under the conditions of pH=0, $P(H_2)$ = 1bar). Maintaining a stable surface may prevent charge transfer on the catalyst-electrolyte interface under the electrochemical condition. In our model, we assumed that the oxidation of water to OH* and O* on Co_3O_4/MnO_2 occurred through the following steps:

$$H_2O + * \rightarrow OH* + H^+ + e^- \qquad \Delta G_1^0 \qquad (1)$$
$$OH* \rightarrow O* + H^+ + e^- \qquad \Delta G_2^0 \qquad (2)$$

Under standard conditions, the free energy of H^+ + e^- is equal to $0.5H_2$. Free energies of all compounds were calculated by:

$$\Delta G^0 = \Delta E + \Delta ZPE - T\Delta S \qquad (3)$$

To include the effects of pH and potential U, eqs 1 and 2 are rewritten as eqs 4 and 5:

$$\Delta G_1 = \Delta G_1^0 - eU - 0.059pH \qquad (4)$$

$$\Delta G_2^0 - eU - 0.059pH \qquad (5)$$

The free energy change of OH* and O* termination can be expressed by eqs 6 and 7:

$$\Delta G_{OH*} = \Delta G_1 \qquad (6)$$

$$\Delta G_{O*} = \Delta G_1 + \Delta G_2 \qquad (7)$$

Table 1. Thermodynamic quantities for 1ML OH*, 1ML O* on Co_3O_4/MnO_2 under standard conditions (pH = 0, $P(H_2)$ = 1 bar, U = 0 V).

surface	ΔE/eV	ΔZPE/eV	TΔS/eV	ΔG/eV
1ML OH*	0.65	-0.09	-0.27	0.83
1ML O*	1.99	-0.23	-0.11	1.87

Table 2. Thermodynamic quantities for 1ML OH*, 0.5ML OH* & 0.5ML O*, 1ML O* on Co_3O_4 under standard conditions (pH = 0, $P(H_2)$ = 1 bar, U = 0 V).

surface	ΔE/eV	ΔZPE/eV	TΔS/eV	ΔG/eV
1ML OH*	1.93	-0.38	-1.03	2.58
0.5ML OH* & 0.5ML O*	4.72	-0.64	-0.74	4.82
1ML O*	7.54	-0.91	-0.45	7.08
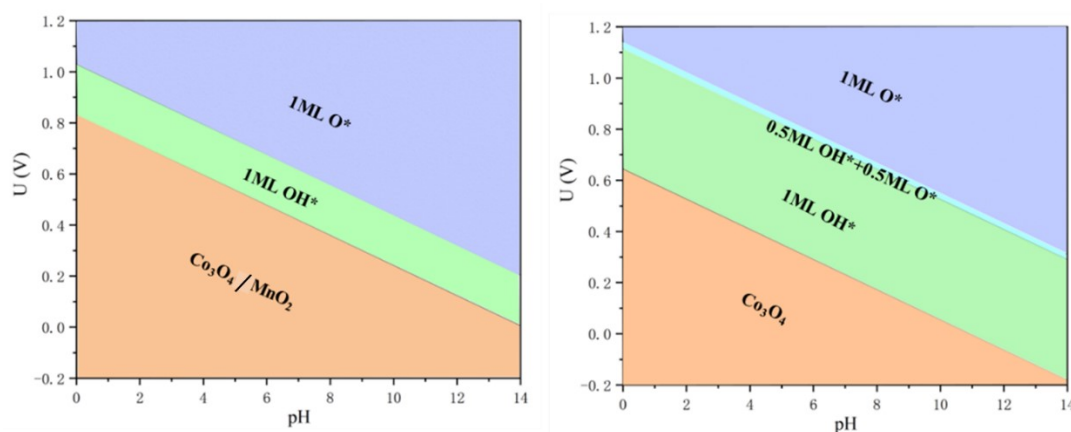
Figure S44. Surface Pourbaix diagrams of Co_3O_4/MnO_2 and Co_3O_4 under electrochemical conditions. The thermodynamically stable states of the surface under SHE and pH values are highlighted by purple (for *O), green (for *OH or O* + OH*), and orange (for substrates).

(45)
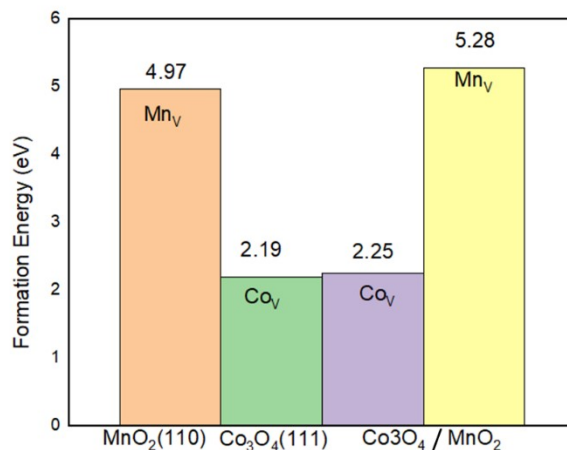
Figure S45. Mn or Co vacancy formation energy.

(46)

The FT-IR spectra were recorded using a Bruker Invenio-S spectrometer with a MCT detector, and an in-situ Harrick chamber. Prior to adsorption of the probes, each sample was pre-treated under Ar (30 mL/min) at 573 K for 30 min in the chamber, then cooled to the room temperature. The background spectrum was then collected. Subsequently, the CO gas was purged into the chamber (30 mL/min) until saturation, with spectra collected at several intervals (0-30 min). After that, the purging gas was switched to high-purity argon for collecting the spectra during desorption (0-30 min).

The results below show the spectra after desorption and background subtraction. For Co_3O_4, the observed bands of surface carbonyl complexes around 2169 and 2130 cm^{-1} agreed well with the literature results.[4] Compared with that of Co_3O_4, the dominant band of MnO_2 shifted to high frequencies, with some bands forming at wave numbers greater than 2200 cm^{-1} (highlighted by yellow circle). This might be related with the higher valence of Mn cations than that of Co cations.[5] Even with Co3+, the corresponding carbonyl bands were reported to be below 2200 cm^{-1}, e.g., typically around 2190 cm^{-1}.[5] As a result, those band around 2200 cm^{-1} could be considered as feature bands of MnO_2. Generally, Co_3O_4/MnO_2 integrated the spectra features of both MnO_2 and Co_3O_4. Compared with MnO_2, the feature bands of MnO_2 around 2200 cm^{-1} (highlighted in yellow) that are absent in Co_3O_4 shift to lower frequencies in Co_3O_4/MnO_2, which implied a lower Mn valence in Co_3O_4/MnO_2 than in MnO_2. This trend was consistent with other characterizations (XAFS, sXAS, XPS) in the manuscript. We further calculated the area of this feature band for both

Co$_3$O$_4$/MnO$_2$ and MnO$_2$, and used the area ratio to estimate the surface coverage of MnO$_2$ in Co$_3$O$_4$/MnO$_2$. The result demonstrated that around 46.8% of Co$_3$O$_4$/MnO$_2$ surface was occupied by Mn sites, yielding a corresponding Mn to Co ratio on the surface to be 0.88, which ratio was consistent with the value of 0.86 obtained by XPS in the manuscript.
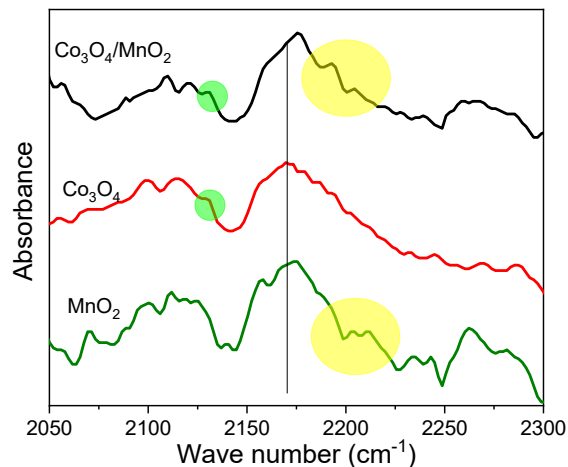
Figure S46. FT-IR spectra of CO adsorption on studied metal oxides, where the green- and yellow-color circle highlight the feature bans attributed to Co$_3$O$_4$ and MnO$_2$, respectively.

(47)
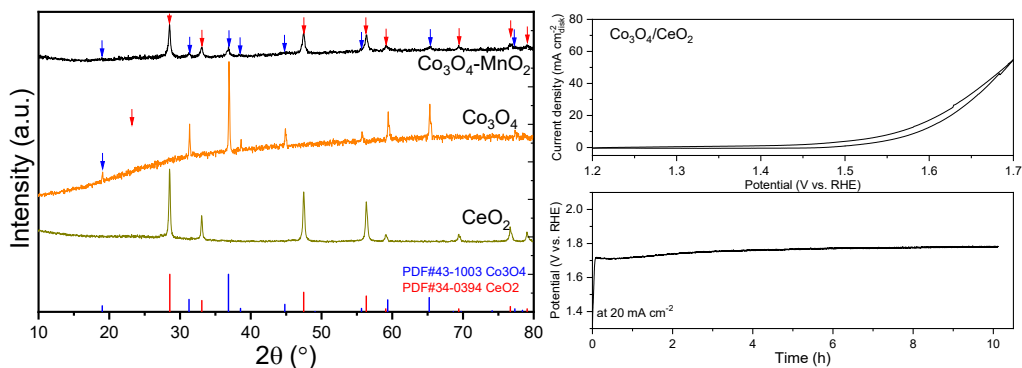
Figure S47. (a) XRD pattern of hybridized Co$_3$O$_4$/CeO$_2$ and (b) its OER performance.

(48)
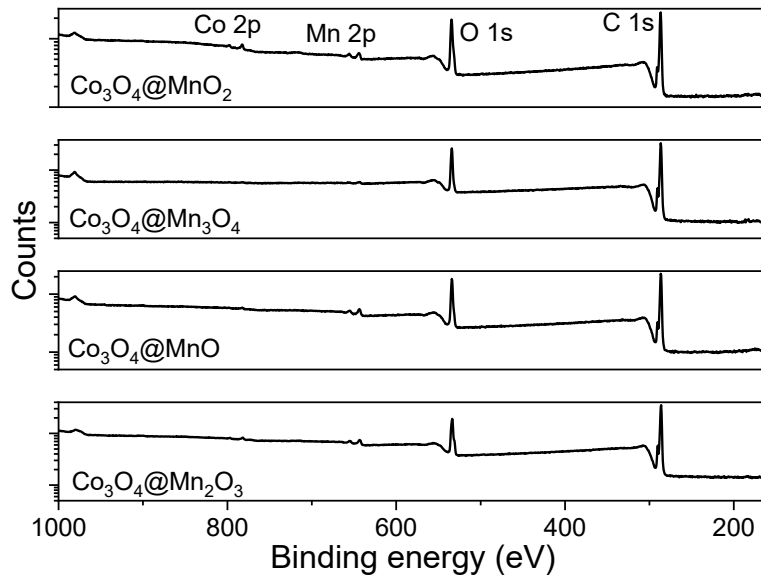
Figure S48. XPS full spectrum of different hybridized Co_3O_4/MnO_x, where Zr 3d XPS signal center around 182 eV was not detected.

(48)

There exists an optimal milling period for the catalytic performance. From the below results, a milling period of 20 hours was optimal to achieve the best OER performance. When the milling period was low, the electronic interaction between Co_3O_4 and MnO_2 might be insufficient to generate beneficial coupling for improving the catalytic performance. This was supported by the XAFS study that elongating the milling period gradually modified the valence and electronic configuration of Co_3O_4 and MnO_2. However, when the milling period is further increased, the crystallinity of the sample might be sacrificed, supported by the TEM image that a milling period of 40 hours generated a disordered structure on the surface of milled Co_3O_4/MnO_2. This sacrificed

crystallinity may influence the interaction of both components within the hybrid and their structural integrity, thus affecting the catalytic activity and stability.
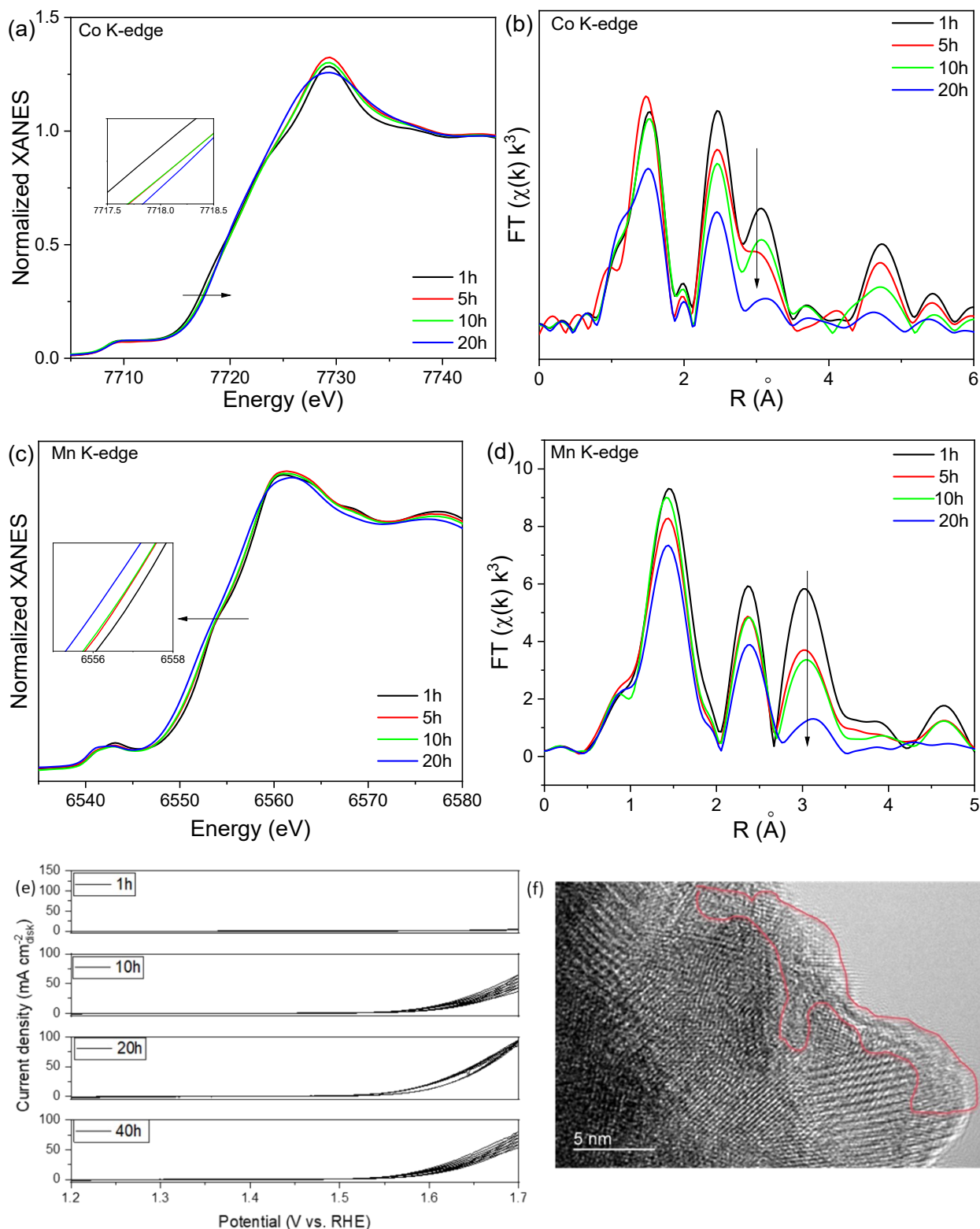
Figure S49. Characterization and OER performance of hybridized Co_3O_4/MnO_2 prepared by ball milling for different time: (a)-(d) Co K-edge and Mn K-edge XAFS; (e) polarization curve; (f) TEM image of hybridized Co_3O_4/MnO_2 milled for 40 hours, where the mass ratio of Co_3O_4 vs. MnO_2 was fixed at 1 : 1.

(49)

We experimented with various mass ratios for MnO_2 versus Co_3O_4, specifically 0.25, 0.5, 1, 2, and 4. The results indicate that a mass ratio of 1 between MnO_2 and Co_3O_4 provides the best OER performance, leading to an atomic ratio of Mn to Co in the hybrid of approximately 0.92.
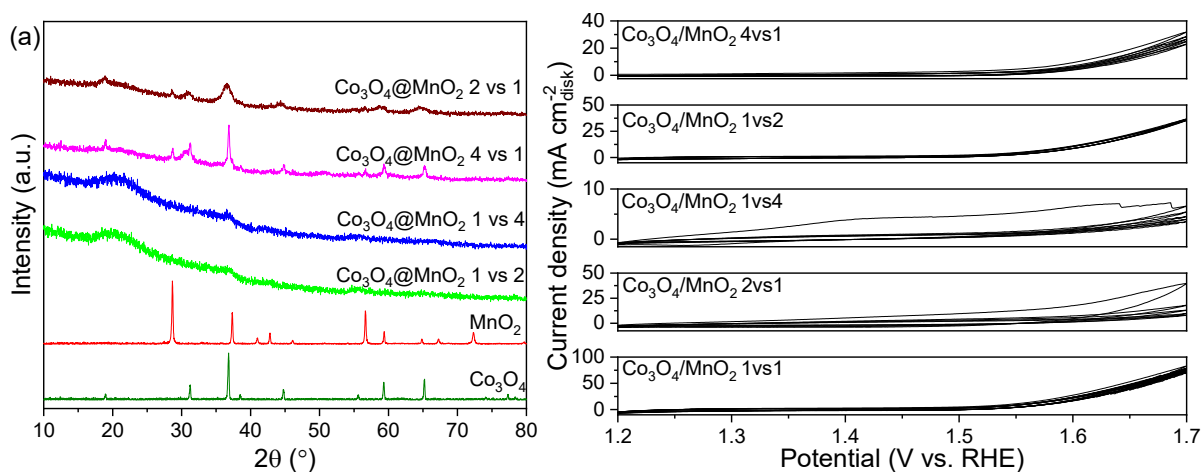
Figure S50. **(a)** XRD and **(b)** CV of Co_3O_4/MnO_2 with different mass ratios. No IR-correction was applied for the CV potentials in 0.5M H_2SO_4.

Part 2: Supplementary Tables:

Supplementary Table 1. OER performance comparison with recently reported catalysts.

Catalyst	Substrate	OER Activity	Test duration	Electrolyte	Source
Co_3O_4/MnO_2	Glassy carbon	10 mA cm^{-2}/319 mV 100 mA cm^{-2}/411 mV	100 hours/varying current up to ~200 mA cm^{-2}	0.5 M H_2SO_4	This work
		10 mA cm^{-2}/311 mV			
		10 mA cm^{-2}/330 mV			
		10 mA cm^{-2}/~353 mV			
		10 mA cm^{-2}/~320 mV			
		10 mA cm^{-2}/~650 mV			
		10 mA cm^{-2}/~360 mV			
		10 mA cm^{-2}/570 mV			
		10 mA cm^{-2}/~300 mV			
		10 mA cm^{-2}/395 mV			
		10 mA cm^{-2}/~670 Mv			
		60 mA cm^{-2}/ 470 mV			
		3 mA cm^{-2}/~310 mV			
		10 mA cm^{-2}/270 mV			
		5 mA cm^{-2}/~320 mV			

Catalyst	Substrate	Activity	Stability	Electrolyte	Reference
RuO_2	Glassy carbon	10 mA cm^{-2}/~210 mV	154 mV increase/100 mA cm^{-2} with 4h test	0.5 M H_2SO_4	This work
RuO_2	Glassy carbon	10 mA cm^{-2}/~210 mV	550 mV increase/10 mA cm^{-2} within 40h test	0.1 M $HClO_4$	Nature Materials 2022[6]
La, Mn doped Co spinel	gold disk	Onset potential starts around 290 mV	~100 mV potential increase / 10 mA cm-2 after 360h test	0.1 M $HClO_4$	Science 2023[7]
IrO_x/$SrIrO_3$	FTO	Onset potential starts around 290 mV	30 hours/10 mA cm^{-2}	0.5 M H_2SO_4	Science 2016[8]
$CoFePbO_x$	Pt/Ti	~7.5 mA cm^{-2}/270 mV	22 hours/varying current up to ~20 mA cm^{-2}	0.1 M H_2SO_4	Nature Catalysis 2019[9]
Ba[Co-POM]/CP	Glassy carbon	~7.5 mA cm^{-2}/270 mV	24 hour/~0.35 mA cm^{-2}	1 M H_2SO_4	Nature Chemistry2018[10]
Co_3O_4/CeO_2	FTO	10 mA cm^{-2}/227 mV	60 mV increase/10 mA cm^{-2} within 50h test	0.5 M H_2SO_4	Nature Communications 2021[11]
$Mn_{7.5}O_{10}Br_3$	Carbon cloth	100 mA cm^{-2}/498 mV	44 mV increase/10 mA cm^{-2} within 500h test	0.5 M H_2SO_4	Nature Communications 2022[12]
Co_2MnO_4	FTO	100 mA cm^{-2}/498 mV	~400 mV increase/100 mA cm^{-2} after 320h test	pH= 1 H_2SO_4	Nature Catalysis 2022[13]
$Ni_{0.5}Mn_{0.5}Sb_{1.7}O_y$	ATO	30 mA cm^{-2}/~330 mV	~65 mV increase/10 mA cm^{-2} after 168h test	1 M H_2SO_4	Energy Environmental Science 2017[14]
N-WC nanoarray	CFP	50 mA cm^{-2}/262 mV	~180 mV increase/10 mA cm^{-2} after 60min test	0.5 M H_2SO_4	Nature Communications 2018[15]
La_2LiIrO_6	Glassy carbon		50 cycles	pH= 1 H_2SO_4	Nature Energy 2017[16]
Li–IrO_x	Glassy carbon		~25 mV increase/10 mA cm^{-2} within 10h test	0.5 M H_2SO_4	J. Am. Chem. Soc. 2019[17]
Electrochemically-polarized IrO_x	/		~50 mV increase/1 mA cm^{-2} within 120h test	0.1 M $HClO_4$	Nature Catalysis 2018[18]
$Sr_{0.85}Na_{0.15}RuO_3$	Glassy carbon		~20 activity loss after 20 CV cycles	0.1 M $HClO_4$	Nature Communications 2019[19]
$Ir_{0.1}Ta_{0.9}O_{2.45}$ NPs	polycrystalline gold		24 h$^\Delta$	0.1 M $HClO_4$	Nature Energy 2022[20]
$SrCo_{0.5}Ir_{0.5}O_3$	Glassy carbon		/	0.1 M $HClO_4$	Science Advances 2022[21]
$RuNi_2$©G-250	Glassy carbon		24 h	0.5 M H_2SO_4	Advanced Materials2020[22]
V−CoP_2/CC	Carbon cloth		24 h/10 mA cm^{-2}	0.5 M H_2SO_4	Angewandte Chemie 2022[23]
Ru/IrO_x	polished gold		24 h/1.55 V	0.05 M H_2SO_4	Chem 2018[24]
SS Pt-RuO2 HNSs	glassy carbon		~90 mV increase/1 mA cm^{-2} within 100h test	0.5 M H_2SO_4	Science Advances2022[25]

Note: Unless additionally noted, the activity listed in the table referred to geometric activity of of the catalyst-modified electrode, which was derived by normalizing OER current by the geometric surface area of the working electrode. $^\Delta$ should reduce the Au electrode every 4 hours at OCP to recover the activity.

References:

1 McCrory, C. C. L., Jung, S., Peters, J. C. & Jaramillo, T. F. Benchmarking Heterogeneous Electrocatalysts for the Oxygen Evolution Reaction. *Journal of the American Chemical Society* **135**, 16977-16987 (2013).

2 Kim, B.-J., Abbott, D. F., Cheng, X., Fabbri, E., Nachtegaal, M., Bozza, F., Castelli, I. E., Lebedev, D., Schäublin, R., Copéret, C., Graule, T., Marzari, N. & Schmidt, T. J. Unraveling Thermodynamics,

Stability, and Oxygen Evolution Activity of Strontium Ruthenium Perovskite Oxide. *ACS Catalysis* **7**, 3245-3256 (2017).

3   Park, J. Y., Kim, H. Y., Kim, Y.-I., Jo, S. Y., Abbas, S. A., Seo, D., Ma, A. & Nam, K. M. Chemical and electrochemical synthesis of cobalt hydroxides: selective phase transformation and application to distinct electrocatalytic reactions. *Journal of Materials Chemistry A* **10**, 12047-12054 (2022).

4   Lin, H.-K., Wang, C.-B., Chiu, H.-C. & Chien, S.-H. In situ FTIR study of cobalt oxides for the oxidation of carbon monoxide. *Catalysis letters* **86**, 63-68 (2003).

5   Hadjiivanov, K. I. & Vayssilov, G. N. Characterization of oxide surfaces and zeolites by carbon monoxide as an IR probe molecule. (2002).

6   Wu, Z.-Y., Chen, F.-Y., Li, B., Yu, S.-W., Finfrock, Y. Z., Meira, D. M., Yan, Q.-Q., Zhu, P., Chen, M.-X., Song, T.-W., Yin, Z., Liang, H.-W., Zhang, S., Wang, G. & Wang, H. Non-iridium-based electrocatalyst for durable acidic oxygen evolution reaction in proton exchange membrane water electrolysis. *Nature Materials* (2022).

7   Chong, L., Gao, G., Wen, J., Li, H., Xu, H., Green, Z., Sugar, J. D., Kropf, A. J., Xu, W., Lin, X.-M., Xu, H., Wang, L.-W. & Liu, D.-J. La- and Mn-doped cobalt spinel oxygen evolution catalyst for proton exchange membrane electrolysis. *Science* **380**, 609-616 (2023).

8   Seitz, L. C., Dickens, C. F., Nishio, K., Hikita, Y., Montoya, J., Doyle, A., Kirk, C., Vojvodic, A., Hwang, H. Y. & Norskov, J. K. A highly active and stable IrO x/SrIrO3 catalyst for the oxygen evolution reaction. *Science* **353**, 1011-1014 (2016).

9   Chatti, M., Gardiner, J. L., Fournier, M., Johannessen, B., Williams, T., Gengenbach, T. R., Pai, N., Nguyen, C., MacFarlane, D. R., Hocking, R. K. & Simonov, A. N. Intrinsically stable in situ generated electrocatalyst for long-term oxidation of acidic water at up to 80 °C. *Nature Catalysis* **2**, 457-465 (2019).

10   Blasco-Ahicart, M., Soriano-López, J., Carbó, J. J., Poblet, J. M. & Galan-Mascaros, J. R. Polyoxometalate electrocatalysts based on earth-abundant metals for efficient water oxidation in acidic media. *Nature Chemistry* **10**, 24-30 (2018).

11   Huang, J., Sheng, H., Ross, R. D., Han, J., Wang, X., Song, B. & Jin, S. Modifying redox properties and local bonding of Co3O4 by CeO2 enhances oxygen evolution catalysis in acid. *Nature Communications* **12**, 3036 (2021).

12   Pan, S., Li, H., Liu, D., Huang, R., Pan, X., Ren, D., Li, J., Shakouri, M., Zhang, Q., Wang, M., Wei, C., Mai, L., Zhang, B., Zhao, Y., Wang, Z., Graetzel, M. & Zhang, X. Efficient and stable noble-metal-free catalyst for acidic water oxidation. *Nature Communications* **13**, 2294 (2022).

13   Li, A., Kong, S., Guo, C., Ooka, H., Adachi, K., Hashizume, D., Jiang, Q., Han, H., Xiao, J. & Nakamura, R. Enhancing the stability of cobalt spinel oxide towards sustainable oxygen evolution in acid. *Nature Catalysis* **5**, 109-118 (2022).

14   Moreno-Hernandez, I. A., MacFarland, C. A., Read, C. G., Papadantonakis, K. M., Brunschwig, B. S. & Lewis, N. S. Crystalline nickel manganese antimonate as a stable water-oxidation catalyst in aqueous 1.0 M H2SO4. *Energy & Environmental Science* **10**, 2103-2108 (2017).

15   Han, N., Yang, K. R., Lu, Z., Li, Y., Xu, W., Gao, T., Cai, Z., Zhang, Y., Batista, V. S., Liu, W. & Sun, X. Nitrogen-doped tungsten carbide nanoarray as an efficient bifunctional electrocatalyst for water splitting in acid. *Nature Communications* **9**, 924 (2018).

16   Grimaud, A., Demortière, A., Saubanère, M., Dachraoui, W., Duchamp, M., Doublet, M.-L. & Tarascon, J.-M. Activation of surface oxygen sites on an iridium-based model catalyst for the oxygen evolution reaction. *Nature Energy* **2**, 16189 (2016).

17   Gao, J., Xu, C.-Q., Hung, S.-F., Liu, W., Cai, W., Zeng, Z., Jia, C., Chen, H. M., Xiao, H., Li, J., Huang, Y. & Liu, B. Breaking Long-Range Order in Iridium Oxide by Alkali Ion for Efficient Water Oxidation. *Journal of the American Chemical Society* **141**, 3014-3023 (2019).

18   Li, T., Kasian, O., Cherevko, S., Zhang, S., Geiger, S., Scheu, C., Felfer, P., Raabe, D., Gault, B. & Mayrhofer, K. J. J. Atomic-scale insights into surface species of electrocatalysts in three dimensions. *Nature Catalysis* **1**, 300-305 (2018).

19   Retuerto, M., Pascual, L., Calle-Vallejo, F., Ferrer, P., Gianolio, D., Pereira, A. G., García, Á., Torrero, J., Fernández-Díaz, M. T., Bencok, P., Peña, M. A., Fierro, J. L. G. & Rojas, S. Na-doped ruthenium perovskite electrocatalysts with improved oxygen evolution activity and durability in acidic media. *Nature Communications* **10**, 2041 (2019).

20   Zheng, Y.-R., Vernieres, J., Wang, Z., Zhang, K., Hochfilzer, D., Krempl, K., Liao, T.-W., Presel, F., Altantzis, T., Fatermans, J., Scott, S. B., Secher, N. M., Moon, C., Liu, P., Bals, S., Van Aert, S., Cao, A., Anand, M., Nørskov, J. K., Kibsgaard, J. & Chorkendorff, I. Monitoring oxygen production on mass-selected iridium–tantalum oxide electrocatalysts. *Nature Energy* **7**, 55-64 (2022).

21   Chen, Y., Sun, Y., Wang, M., Wang, J., Li, H., Xi, S., Wei, C., Xi, P., Sterbinsky, G. E., Freeland, J. W., Fisher, A. C., Ager, J. W., Feng, Z. & Xu, Z. J. Lattice site–dependent metal leaching in perovskites toward a honeycomb-like water oxidation catalyst. *Science Advances* **7**, eabk1788 (2021).

22   Cui, X., Ren, P., Ma, C., Zhao, J., Chen, R., Chen, S., Rajan, N. P., Li, H., Yu, L., Tian, Z. & Deng, D. Robust Interface Ru Centers for High-Performance Acidic Oxygen Evolution. *Advanced Materials* **32**, 1908126 (2020).

23   Wang, Y., Jiao, Y., Yan, H., Yang, G., Tian, C., Wu, A., Liu, Y. & Fu, H. Vanadium-Incorporated CoP2 with Lattice Expansion for Highly Efficient Acidic Overall Water Splitting. *Angewandte Chemie* **134**, e202116233 (2022).

24   Shan, J., Guo, C., Zhu, Y., Chen, S., Song, L., Jaroniec, M., Zheng, Y. & Qiao, S.-Z. Charge-Redistribution-Enhanced Nanocrystalline Ru@IrOx Electrocatalysts for Oxygen Evolution in Acidic Media. *Chem* **5**, 445-459 (2019).

25   Wang, J., Yang, H., Li, F., Li, L., Wu, J., Liu, S., Cheng, T., Xu, Y., Shao, Q. & Huang, X. Single-site Pt-doped RuO_2 hollow nanospheres with interstitial C for high-performance acidic overall water splitting. *Science Advances* **8**, eabl9271 (2022).